Dalton Transactions

ROYAL SOCIETY OF CHEMISTRY

PAPER

View Article Online
View Journal | View Issue

Check for updates

Cite this: *Dalton Trans.*, 2023, **52**, 15394

Electrocatalytic reduction of CO_2 to CO by a series of organometallic Re(I)-tpy complexes†

Shriya Saha, [a] Thomas Doughty, [b] Dibyendu Banerjee,[c] Sunil K. Patel, [a] Dibyendu Mallick, *[c] E. Siva Subramaniam Iyer, [a] Souvik Roy *[b] and Raja Mitra *[a]

Received 11th February 2023,
Accepted 27th April 2023

DOI: 10.1039/d3dt00441d

rsc.li/dalton

A series of organometallic Re(I)(**L**)$(CO)_3$Br complexes with 4′-substituted terpyridine ligands (**L**) has been synthesised as electrocatalysts for CO_2 reduction. The complexes' spectroscopic characterisation and computationally optimised geometry demonstrate a facial geometry around Re(I) with three *cis* COs and the terpyridine ligand coordinating in a bidentate mode. The effect of substitution on the 4′-position of terpyridine (**Re1–5**) on CO_2 electroreduction was investigated and compared with a known Lehn-type catalyst, Re(I)(bpy)$(CO)_3$Br (**Re7**). All complexes catalyse CO evolution in homogeneous organic media at moderate overpotentials (0.75–0.95 V) with faradaic yields of 62–98%. The electrochemical catalytic activity was further evaluated in the presence of three Brønsted acids to demonstrate the influence of the pK_a of the proton sources. The TDDFT and ultrafast transient absorption spectroscopy (TAS) studies showed combined charge transfer bands of ILCT and MLCT. Amongst the series, the Re-complex containing a ferrocenyl-substituted terpyridine ligand (**Re5**) shows an additional intra-ligand charge transfer band and was probed using UV-Vis spectroelectrochemistry.

Open Access Article. Published on 03 2566. Downloaded on 6/2/2569 0:03:00.
This article is licensed under a Creative Commons Attribution-NonCommercial 3.0 Unported Licence.

Introduction

Carbon dioxide (CO_2), one of the planet's most essential carbon sources, is also one of the key greenhouse gases contributing to global warming.[1] Despite the existence of a natural carbon cycle that maintains the CO_2 level in the atmosphere, the addition of an uncontrollable amount of anthropogenic CO_2 is tilting the balance of CO_2 in the Earth's atmosphere slowly but steadily in the wrong direction.[2–5] The recent decline of CO_2 emissions during the global pandemic in 2020 [3] suggests a need to either find sustainable alternatives to fossil fuel (*e.g.* green H_2) or upcycle the CO_2 to fuel and feedstock to realise a carbon-neutral cycle. Without readily available alternative fuel sources, the dependence on fossil fuels cannot be eliminated drastically.[6] Considering the current scenario, electroreduction presents a promising route to CO_2 recycling for the production of value-added chemicals (CO, $HCOO^-$) or carbon-neutral fuels (CH_4, CH_3OH).[7–10]

Nevertheless, the reduction of CO_2 is associated with a high activation energy barrier due to the highly stable C═O bonds. One of the most prominent ways to overcome the high activation barrier is by an electrochemical reduction in the presence of a catalyst.[11–16] In natural enzymatic systems, such as CO-dehydrogenase (CODH), CO_2 activation is facilitated by hydrogen bonding interactions. This has inspired the molecular design of synthetic CO_2R catalysts that involves tuning both the primary and secondary coordination spheres to modulate the electronic properties and harness intramolecular through-space interactions for improved activity. The tuneability of the ligand frameworks in transition metal complexes allows the introduction of tailored functional groups in the outer sphere that can promote selective CO_2 reduction. Recently, a wide range of CO_2R catalysts containing secondary sphere functionalities has been reported, such as cobalt–phosphine complexes with pendant amines,[17] iron porphyrins with pendant phenols,[18] phthalocyanines with trimethylammonium groups,[19] and cobalt aminopyridine macrocycles.[20]

Since the discovery of the CO_2R activity of *fac*-Re(I)(bpy)$(CO)_3$X (X = Cl/Br) complexes by Lehn and coworkers, a range of Re(I)- and Mn(I)-carbonyl complexes with bidentate diamine N–N ligands have been synthesised and studied for electrochemical CO_2-to-CO conversion.[21–28] Among these molecular catalysts, 2,2′-bipyridine (bpy) and 1,10-phenanthroline (phen) remain the most widely used ligands.[22,29–35] In particular, Re

[a]*School of Chemical and Materials Sciences, Indian Institute of Technology Goa, Farmagudi, Goa 403401, India. E-mail: rajamitra@iitgoa.ac.in*
[b]*School of Chemistry, University of Lincoln, Green Lane, Lincoln, Lincolnshire, LN6 7DL, UK. E-mail: sroy@lincoln.ac.uk*
[c]*Department of Chemistry, Presidency University, Kolkata 700073, India. E-mail: dibyendu.chem@presiuniv.ac.in*

† Electronic supplementary information (ESI) available. See DOI: https://doi.org/10.1039/d3dt00441d

This journal is © The Royal Society of Chemistry 2023

Open Access Article. Published on 03 2566. Downloaded on 6/2/2569 0:03:00.
This article is licensed under a Creative Commons Attribution-NonCommercial 3.0 Unported Licence.

$(bpy)(CO)_3Cl$ has been demonstrated to display good selectivity towards CO evolution under electrochemical and light-driven conditions but with low catalytic rate constants and deactivation *via* dimerisation. To improve the performance of Re- and Mn-diimine systems, the direct electronic effect has been investigated by modifying the diimine ligand in the primary coordination sphere to introduce electron-donating or electron-withdrawing substituents.[36–40] The outer-sphere interactions have also been exploited for Re- and Mn-diimine systems.[39] Recent work on Mn and Re catalysts with bipyridine ligand scaffolds decorated with primary amines, hydroxyls, pendant imidazole and a thiourea tether shows a significant influence of the donor groups on CO_2-to-CO activity.[33,41–47]

We envisioned that using substituted terpyridines (tpy) as the ligand offers a handle to tune the primary and secondary coordination structures in tandem. Terpyridine can coordinate to a $[Re(CO)_3X]$ unit in a robust bidentate fashion, leaving a pendant pyridine group near the active site.[48] During catalysis, this pendant pyridine can facilitate CO_2 activation in the protonated form, while the substituents on the terpyridine ligand can impact the electronics of the metal centre. A few Re(tpy)$(CO)_3X$ (X = Cl/Br) derivatives have been reported in the literature, but those have rarely been investigated for electrocatalytic CO_2 reduction, despite their structural similarity to Lehn-type Re(bpy)$(CO)_3X$ catalysts.[49–51] Structural characterisation of these complexes typically shows a *facial* arrangement of a bidentate tpy ligand and three COs.[52,53] The uncoordinated pyridyl ring is forced to stay non-coplanar with the other two coordinated pyridine rings due to the sterically crowded Re(I) centre. Re(tpy)$(CO)_3X$ compounds show photochemical properties such as UV emitter, fluorescence, and NIR-emitter.[54–58]

Herein, we report the synthesis and electrocatalytic properties of a series of *fac*-Re(I)(**L**)$(CO)_3Br$ complexes containing 4′-substituted-2,2′:6′,2″-terpyridine ligands (**L**). Five Re-complexes (**Re1–5**) containing 4′-substituents with varying electronic properties were synthesised, and their structures are shown in Fig. 1. The electrochemical CO_2R activity of **Re1–5** was compared with the well-known Lehn's catalyst, *fac*-Re(bpy)$(CO)_3Br$ (**Re7**). This study demonstrates the effect of a pendant pyridine ring and a range of 4′-substituents on the tpy ligands on CO_2 reduction. A ferrocenyl-appended Re(I) compound (**Re5**) was also synthesised and studied using electrochemical techniques to understand the effect of the ferrocenyl moiety as multiple metal centres are known to alter the electrochemical and catalytic activities. This study explores the usefulness of having additional metal centres attached to terpyridine ligands at the 4′ position for the CO_2R studies. The electrocatalytic investigations are complemented with computational studies, transient absorption spectroscopy (TAS) and spectroelectrochemistry to elucidate the mechanistic aspect of the electrochemical processes.

Results and discussion

Synthesis and characterisation

All ligands with a substitution (aryl or ferrocenyl) on the 4′ position of 2,2′:6′,2″-terpyridine were synthesised using the modified Krönke pyridine synthesis that was reported by Hanan and co-workers (**L2–5**).[59] Improved yields were obtained by refluxing the mixture for 12 h and using excess ammonia (50 instead of 2.5 equivalent). In most cases, the ligands precipitate out from the clear orange-coloured solution during the reaction due to the low solubility of the products (**L2–4**) in ethanol. Interestingly, the ligand **L5** was obtained with a lower yield due to being more soluble in ethanol than other ligands. The yield of **L5** was significantly improved by cooling the reaction mixture at 4 °C for 24 h. However, cooling had a minimal effect on the yield for other ligands (**L2–4**). The analytical data for precipitated ligands showed sufficient purity for further reaction.

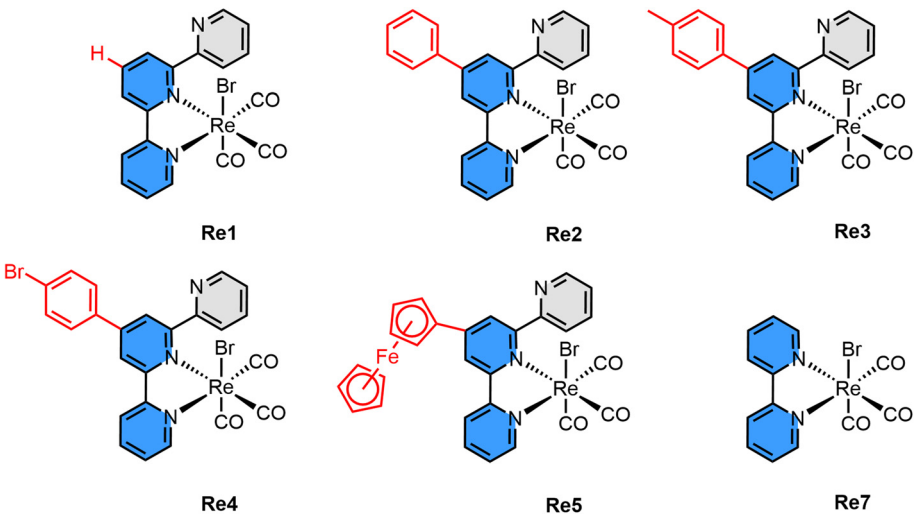

Fig. 1 Molecular structure of Re(I) complexes used as a catalyst in this study. **Re7** is used as a standard for comparison.

Open Access Article. Published on 03 2566. Downloaded on 6/2/2569 0:03:00.
This article is licensed under a Creative Commons Attribution-NonCommercial 3.0 Unported Licence.

Rhenium(I) complexes were synthesised by refluxing $Re(CO)_5Br$ and ligands in dry toluene for 1–4 h following literature procedures (Scheme 1). All complexes, except **Re5**, precipitated as microcrystalline solids during the reaction or upon cooling to room temperature, with a yield of 56–98% (**Re1–4**). Compound **Re5** was isolated in 74% yield that includes ~0.5 molecules of toluene as a solvent of crystallisation (*vide infra*). The toluene was consistently present in different batches of synthesis. Complexes were characterised by infrared spectroscopy (IR), ^{1}H NMR, mass spectroscopy, UV-Vis spectroscopy and elemental analysis (data can be found in ESI, Fig. S1–S9†).

The ^{1}H NMR spectra in $CDCl_3$ of the rhenium complexes show the deshielding of the ligand's pyridine protons, suggesting the coordination of terpyridine ligands to the Re(I) centre. The ^{1}H NMR of the ligands shows a symmetric pattern due to the inherent plane of symmetry present on them, which is not observed in the proton NMR of the metal complexes, indicating that the metal has coordinated with the ligand in a κ^2-NN coordination mode.[60,61] Because of the κ^2-NN coordination, one pyridine ring is available for further secondary interactions. The ^{13}C peaks for CO ligands were not observed in the $CDCl_3$ solvent for all Re complexes. Interestingly, the ^{13}C peak corresponding to CO ligands was observed in DMSO-d_6 solvent; hence, NMR was reported in both solvents. ^{1}H NMR of **Re5** showed three additional peaks at 7.24, 7.17 and 2.30 ppm in DMSO-d_6, which upon analysis were found to be of toluene, confirmed by 2D NMR (see ESI†) and reported literature values.[62] From ^{1}H NMR, it was found out ~0.5 molecule of toluene is present per molecule of the complex and it is present as a solvent of crystallisation.

IR comparison studies are carried out to probe the κ^2-NN coordination further (Fig. 2). The presence of three carbonyl stretches confirms κ^2-NN coordination and is consistent with the *cis* arrangement of the CO ligands, as reported in the recent literature.[63] The starting material $Re(CO)_5Br$ shows two

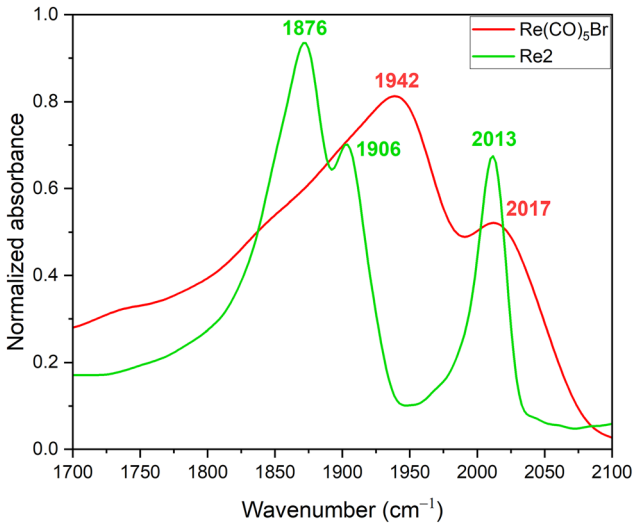

Fig. 2 Representative partial ATR-IR (2100–1700 cm^{-1}) comparison of the starting precursor, $Re(CO)_5Br$, and the 4′-phenyl-2,2′:6′,2″-terpyridine ligand-coordinated Re(I) complex, **Re2**. The complete range of ATR-IR spectra can be found in the ESI.†

IR active $\nu_{str(C\equiv O)}$ bands, which are assigned A_1 (2017 cm^{-1}) for the CO present in the axial position and a doubly degenerate E (1942 cm^{-1}) for the other four CO in the equatorial position.[64] With the coordination of the terpyridine unit to the Re(I) centre, three carbonyl frequencies are observed that are charcteristic of *facial* tricarbonyl complexes. The higher energy band, A_1, does not shift significantly for **Re1–5** (*cf.* 2017 cm^{-1} to 2013–2021 cm^{-1}). The lower energy degenerate E band splits into two bands due to the presence of κ^2-NN from the terpyridine derivatives (Fig. S10†).[30] The shift in $\nu_{str(C\equiv O)}$ frequency, particularly for the E band, for **Re1–5** compared with the $Re(CO)_5Br$ can be attributed to the better back-donation from the Re(I) metal centre to the π^* orbital of CO due to the increase in electron density on the metal centre. NMR and FTIR studies

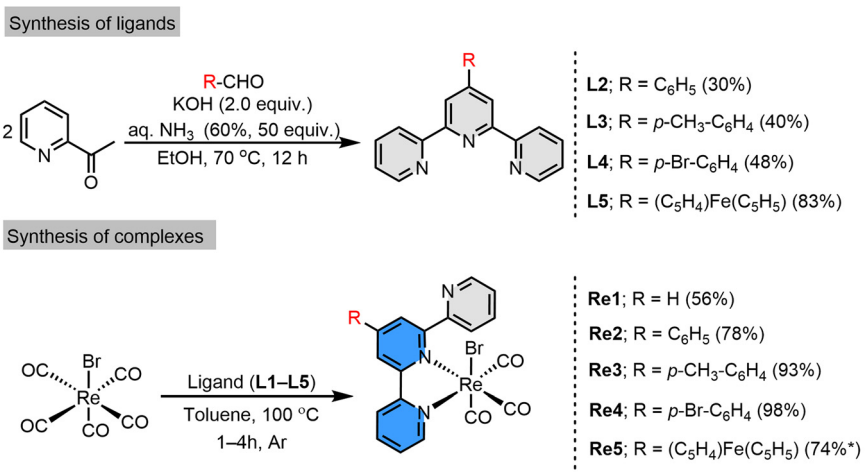

Scheme 1 Synthesis of terpyridine ligands (**L2–5**) and *fac*-Re(I)(L)$(CO)_3$Br complexes (**Re1–5**), where **L** = **L1–5**. ***Re5** contains toluene (~0.5 molecules, calculated from ^{1}H NMR) as a solvent of crystallisation.

This journal is © The Royal Society of Chemistry 2023

Open Access Article. Published on 03 2566. Downloaded on 6/2/2569 0:03:00.
This article is licensed under a Creative Commons Attribution-NonCommercial 3.0 Unported Licence.

Table 1 Experimental and calculated absorption properties of ligands and the corresponding Re(I) complexes. TDDFT data were calculated at the B3LYP/def2-TZVP level of theory using acetonitrile as an implicit solvent

Ligands λ_{max} /nm (10^3 ε/L mol^{-1} cm^{-1})		Prediction from TDDFT calculation λ_{max}/nm (oscillator strength)	Re(I) complexes λ_{max}/nm (10^3 ε/L mol^{-1} cm^{-1})		Prediction from TDDFT calculation λ_{max}/nm (oscillator strength)
In DMF	In acetonitrile	In acetonitrile	In DMF	In acetonitrile	In acetonitrile
L1:	**L1:**	**L1:**	**Re1:**	**Re1:**	**Re1:**
279 (37.8)	235 (28.7)	235 (0.412)	309 (20.9)	247 (21.5)	249 (0.180)
329 (4.36)	277 (33.1)	283 (0.323)	375 (5.58)	310 (15.5)	256 (0.146)
				372 (2.80)	303 (0.393)
					431 (0.056)
L2:	**L2:**	**L2:**	**Re2:**	**Re2:**	**Re2:**
309 (25.3)	252 (23.0)	229 (0.274)	384 (9.27)	266 (47.6)	281 (0.355)
	275 (22.5)	264 (0.312)		380 (7.08)	309 (0.287)
	329 (1.8)				438 (0.088)
L3:	**L3:**	**L3:**	**Re3:**	**Re3:**	**Re3:**
278 (25.3)	253 (28.0)	228 (0.33)	307 (23.9)	268 (28.6)	287 (0.328)
316 (10.2)	278 (31.1)	261 (0.21)	382 (4.30)	301 (29.3)	309 (0.227)
	332 (1.5)	274 (0.31)		379 (4.91)	436 (0.098)
		285 (0.53)			
L4:	**L4:**	**L4:**	**Re4:**	**Re4:**	**Re4:**
275 (32.3)	253 (28.1)	231 (0.28)	305 (32.6)	269 (53.7)	285 (0.437)
312 (7.36)	276 (30.8)	262 (0.25)	388 (5.84)	297 (54.4)	310 (0.211)
	330 (2.5)	282 (0.58)		378 (8.50)	441 (0.095)
L5:	**L5:**	**L5:**	**Re5:**	**Re5:**	**Re5:**
283 (17.9)	250 (17.1)	267 (0.174)	311 (42.1)	256 (23.4)	282 (0.260)
363 (1.29)	280 (17.8)	282 (0.318)	370 (10.6)	310 (21.8)	309 (0.197)
459 (0.56)	365 (0.83)	380 (0.015)	516 (5.62)	367 (5.02)	438 (0.098)
	460 (0.26)	506 (0.002)		516 (2.35)	516 (0.008)
					602 (0.013)

suggest that the complexes most probably stay in a distorted octahedral geometry, and all CO are *cis* in nature; hence all complexes are *facial* isomers.

The UV-Vis spectra of ligands and metal complexes were recorded in organic solvents (DMF and acetonitrile, Table 1). The ligands and the Re(I) complexes showed similar absorption spectra in DMF and acetonitrile. The spectral features are typical of the rhenium complexes and the terpyridine ligands reported earlier. The higher energy transition band from 250 nm to 350 nm is assigned to $\pi \rightarrow \pi^*$ transition in the terpyridine ligand. A bathochromic shift ~30 nm is observed for Re complexes compared with the pure ligands that was ascribed to N^N ligand-centred $\pi \rightarrow \pi^*$ transitions (307–388 nm in acetonitrile) (Table 1).[53,65,66]

The **Re5** complex shows a broad absorption band at λ_{max} around 516 nm that extends up to 650 nm, which might have originated due to the presence of the ferrocenyl moiety. Compared with **L5** (λ_{max} = 460 nm) and free ferrocene (λ_{max} = 440 nm), the bands for **Re5** are substantially redshifted, which can be attributed to the extended conjugation of the ferrocene unit. The oscillator strength obtained from TDDFT studies agrees with the molar absorption coefficient (Table 1). TDDFT and ultrafast transient absorption spectroscopy studies were carried out to understand the absorption properties further assigned to the metal-to-ligand charge transfer (MLCT) and intra-ligand charge transfer (ILCT) processes within the metal complexes. Compounds **Re1–5** showed no significant changes in the UV-Vis spectra even after 24 h, suggesting the stability of those compounds in acetonitrile (Fig. S11†).

The crystal obtained for **Re5** is always associated with clusters or overlapping crystals unsuitable for single-crystal X-ray diffraction. A computational geometry-optimised structure for all was obtained using DFT calculation (*vide infra*) to understand the structural aspect of those Re(I) compounds. One of the representative DFT-optimised structures is shown in Fig. 3. It shows that the Re(I) is in an octahedral environment with terpyridine serving as a bidentate ligand, and all CO ligands are co-ordinated in a *cis* orientation.

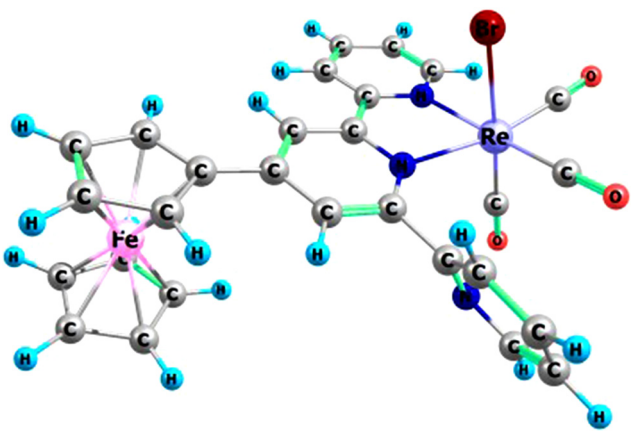

Fig. 3 The DFT optimised structure of **Re5** at the B3LYP/def2-TZVP level of theory.

Open Access Article. Published on 03 2566. Downloaded on 6/2/2569 0:03:00.
This article is licensed under a Creative Commons Attribution-NonCommercial 3.0 Unported Licence.

TDDFT studies

TDDFT calculations have been performed to investigate the photochemical properties of the complexes **Re1–5**. The major optical transitions above 250 nm with an oscillator strength $f >$ 0.005 are tabulated in Fig. S12–S16.† The peak around 431 nm in **Re1** originates due to the transition from HOMO−1, which is composed of $5d_{yz}$ (Re) and $4p_y$(Br) orbitals, to LUMO, *i.e.*, the π*(tpy) orbital. Therefore, the band around 431 nm could be attributed to a metal-to-ligand charge transfer (MLCT) band. The MLCT band is slightly red-shifted (436–441 nm) for the complexes **Re2**, **Re3** and **Re4**. Interestingly, for **Re5**, the MLCT band was observed at 438 nm, which predominantly arises due to the transitions from HOMO and HOMO−1 to LUMO, which is the π*(fctpy) orbital. The HOMO of **Re5** is composed of the $3d_{xy}$ (Fe) orbital, and the HOMO−1 is similar to the HOMO−1 of other rhenium complexes (**Re1–4**). Hence, the peak around 438 nm for **Re5** can be characterised as a combination of intra-ligand charge transfer (ILCT) and MLCT transitions. The absence of the band around 438 nm for the **L5** ligand further suggests the MLCT nature of this peak for the **Re5** complex. A highly intense band is observed around the 303–309 nm region for all these complexes (**Re1–5**), which arises due to a combination of π(R-tpy) to π*(R-tpy) and π_{yz}(Re–Br) to π*(R-tpy) transitions and hence can be assigned to a mixed ILCT and MLCT band. The most intense band is observed around 280 nm for all the complexes except **Re1**, which has the most intense band around 250 nm. The appearance of the 280 nm band for complexes **Re2–5** is due to the transition from an orbital composed of $4p_y$(Br) and π(R-tpy) to the π*(R-tpy) orbital. A similar transition is responsible for the 250 nm band in the **Re1** complex. Two additional low-intensity bands observed around 516 nm and 602 nm regions for the **Re5** complex arise due to d–d transitions from the ferrocene moiety of the fctpy ligand (**L5**). These bands are also found at 506 nm and 587 nm for the **L5** ligand.

Ultrafast transient absorption spectroscopy

The femtosecond transient absorption spectra resulting from the 320 nm (3.8 eV) pump and whitelight (350 nm to 650 nm) probe of **Re1** and **Re5** are shown in Fig. 4, while those of **Re2** to **Re4** are shown in Fig. S18–S20.† All measurements are performed in acetonitrile. The transients of **Re1** to **Re4** are dominated by excited state absorption (ESA) signals in the entire spectral range measured. The TA spectra of **Re1** to **Re4** reveal two distinct bands. One is a sharp band at <400 nm and a broad spectrum beyond 400 nm. The ESA at lower wavelengths exhibits a sharp peak at 375 nm for **Re1** and around 365 nm for **Re2**, **Re3**, and **Re4**. This band is ascribed to the excitation to a higher energy state of the radical anion state of the terpyridine ligand resulting from charge transfer from the metal centre to the ligand. This assignment is reasonable as earlier reports on analogous molecules have shown similar features; *e.g.* the transient absorption of bipyridine (bpy) rhenium(I) analogue [Re(bpy)(CO)$_3$Cl] also shows an ESA at 373 nm,

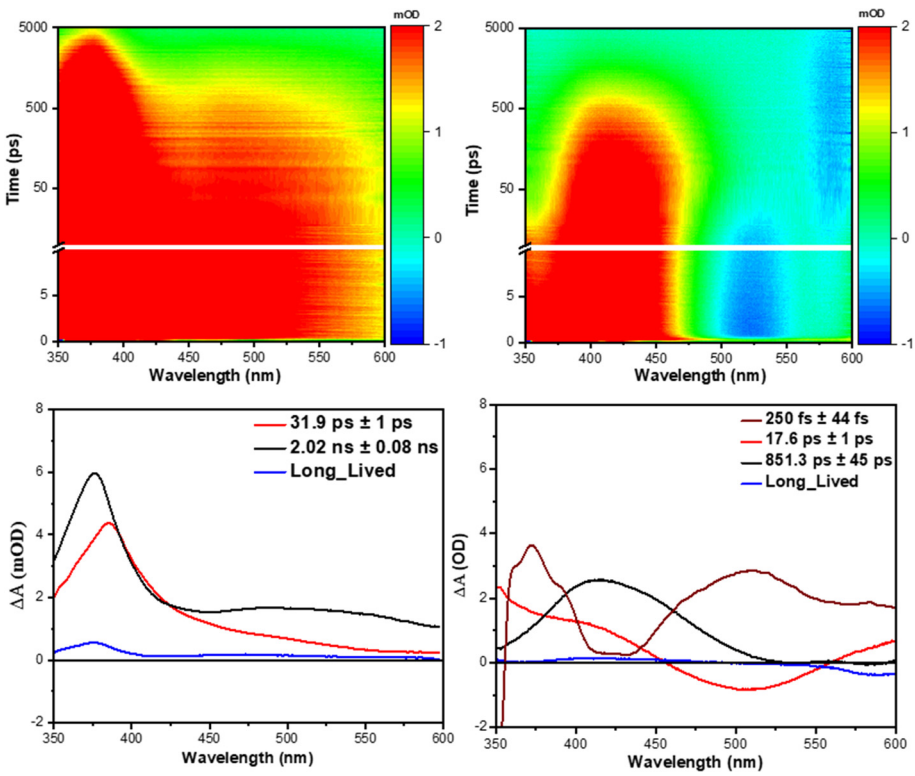

Fig. 4 2D contour plots of the transient absorption spectra of **Re1** (a) and **Re5** (b) measured in acetonitrile after 320 nm excitation and the corresponding globally fitted lifetime data in (c) and (d).

This journal is © The Royal Society of Chemistry 2023

Open Access Article. Published on 03 2566. Downloaded on 6/2/2569 0:03:00.
This article is licensed under a Creative Commons Attribution-NonCommercial 3.0 Unported Licence.

which has been assigned to $bpy^{\bullet-}$.[65,67,68] A similar ESA in the sub-400 nm [Re(R-tpy-κ^2N)(CO)$_3$Cl] range is assigned to the ligand where the charge is concentrated over the bipyridine part of the ligand.[65] The broad ESA in the mid-visible region (450 nm–600 nm) is assigned to the excitation of the MLCT state to higher states.[69] A broad excited state absorption band from 450 nm to 600 nm in [Re(R-tpy-κ^2N)(CO)$_3$Cl] has been assigned to the lowest triplet MLCT state.[67,68,70,71]

The TA of **Re5** has significantly different characteristics and warrants further investigation compared with the **Re1** to **Re4** complexes. Although the high-energy ESA is observed in the rest of the molecules studied in this work, this band is significantly red-shifted. This can be ascribed to the enhanced conjugation of the terpyridine ligand with ferrocene. Based on earlier work and the TDDFT calculations, the high energy band is assigned to a $\pi \rightarrow \pi^*$ transition. The ferrocene is attached to the terpyridyl group directly through the cyclopentadienyl groups. Hence the red-shift of this band due to extended conjugation is trivial. However, unlike **Re1** to **Re4**, where the ESAs of the MLCT states are observed, in **Re5**, this spectral region is dominated by two distinct negative signals (stimulated emission, SE). This is clearly due to the presence of the ferrocene moiety.[72,73] It must be emphasised that the stimulated emission results only in the Re complex. In the presence of the ferrocene moiety in **Re5**, the MOs of the Re moiety, along with the 3d orbitals of the Fe, contribute to the MOs (Fig. S16†). This might lead to additional states in the complex and manifests as seen from the evolution of new negative bands centred at 590 nm in the transient spectra of the **Re5** complex. Such a state is missing in the **L5** compound (Fig. S21†). This new state might stabilise the ^{3}CT state, which exhibits stimulated emission at a longer delay.

Interestingly, one of the negative bands develops only after 10 ps of the excitation by the pump pulse. At the pump wavelength of 320 nm, the direct excitation of ferrocene is inevitable. The initial negative signal centred at 525 nm closely matches the charge transfer band of lone ferrocene. It remains to be ascertained whether this band is a bleach signal or a stimulated emission from the ferrocene moiety. It is noteworthy that when the TA measurements are performed on ligand **L5**, no negative band is observed at these wavelengths. Had it been a ground-state bleach signal from the ferrocenyl group, such a state would have been observed in **L5** as well (Fig. S21†). The computational calculations described in the earlier sections reveal the mixing of various orbitals of the two metal ions present in the molecule, which alter the MOs. Such mixing can result in the stabilisation of certain energy levels that are otherwise short-lived. In this experiment, the molecules are excited to energy states higher than the lowest energy transitions. Such a state can populate the CT state arising from ferrocene. This state is depopulated by the whitelight probe and appears as stimulated emission in the TA spectra of **Re5**, shown in Fig. 4. The emission band at 525 nm is also due to the presence of Re in the **Re5** because it is not arising in the transient absorption of the ligand (**L5**) (Fig. S21†).

Unlike **Re1** to **Re4**, the ILCT band is significantly redshifted in **Re5** and can be attributed to enhanced conjugation resulting in a lowering of the energy gaps among the excited states. The ESA band in **Re5** consequently has a peak at 415 nm. The most interesting feature is the appearance of a strong stimulated emission centred at 590 nm. This band evolves only beyond 10 ps post excitation. This shows that a new band is developed from the locally excited states and could not be formed from the direct excitation of any ground states. If this new band were the result of direct excitation, the signal would have evolved much earlier. The TDDFT investigations suggest a mixed nature of ILCT and MLCT transitions in **Re5**.

The wavelength-dependent kinetic traces were analysed to understand the excited states' evolution, and global analyses were performed to obtain the decay-associated spectra. The global lifetime analysis spectra for **Re1** and **Re5** are given in Fig. 4(c and d), and the other compounds are in Fig. S18–S20.† The time constants at a few representative wavelengths are tabulated in Fig. S17–S20.† The evolution-associated decay spectra show that three main components characterised by distinct time constants can explain the excited state dynamics in these compounds. The TA features of **Re1–4** are similar to the earlier reports on the structurally analogous [Re(C_6H_5-tpy-κ^2N)(CO)$_3$Cl].[74]

The various excited state processes are pictorially represented in a Jablonski diagram in Fig. 5. Upon 320 nm excitation, the molecules are excited to a ^{1}MLCT state and then undergo intersystem crossing forming a hot triplet state within <200 fs. This evolution is missed in our experiments due to the instrument response. This nascent triplet state relaxes by internal vibrational relaxation, eventually forming a relaxed triplet ^{3}MLCT state within a few picoseconds. This process takes place in ~30 ± 1 ps for **Re1**, whereas for **Re2–4**, it is slower. The longer relaxation time for **Re2–4** can be attributed to an enhanced conjugation upon substitution. The ^{3}MLCT returns to the ground state by non-radiative pathways over the next few ns. These states appear as long-lived components in the global spectra (Fig. 4(c)).

In **Re5**, the TA measurements indicate that alternative pathways of de-excitation of the triplet state open up. We have observed an additional component appearing as a stimulated emission in **Re5**, as shown in Fig. 4(d). This additional state is formed possibly due to extensive long-range coupling between the orbitals of ferrocene and rhenium in the **Re5** complex (Fig. S20†). This contention is bolstered by the theoretical investigations where the mixing of orbitals of the states

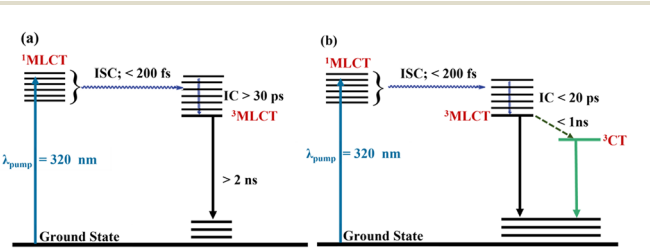

Fig. 5 Proposed deactivation mechanism of excited state Re-complexes (**Re1** to **Re4**) in (a) and **Re5** in (b).

Open Access Article. Published on 03 2566. Downloaded on 6/2/2569 0:03:00.
This article is licensed under a Creative Commons Attribution-NonCommercial 3.0 Unported Licence.

involved in electronic transitions is observed. In addition to the fast internal conversion in <200 fs, a significantly fast ~17 ± 1 ps process is observed in **Re5**. The shorter lifetime of the vibrationally relaxed state can be associated with the additional process leading to the formation of the mixed state. This new state is evolved in the presence of a ferrocenyl unit, which is long-lived and can alter the photo- and electrocatalytic activities of the rhenium complexes.[75]

Electrochemical properties

To assess the redox property of the complexes under noncatalytic conditions, cyclic voltammetry (CV) was performed in N_2-saturated acetonitrile solutions containing a ~0.6 mM Re-complex (0.5 mM for **Re3** due to its lower solubility) and 0.1 M *n*-Bu_4NBF_4 supporting electrolyte at different scan rates (Fig. 6 and Fig. S22–S26†). All reported potentials are referenced against the ferrocene ($Fc^{+/0}$) couple. The reduction potentials and diffusion coefficients (derived from scan rate-dependent CVs, Fig. S27†) for the complexes are summarised in Table 2.

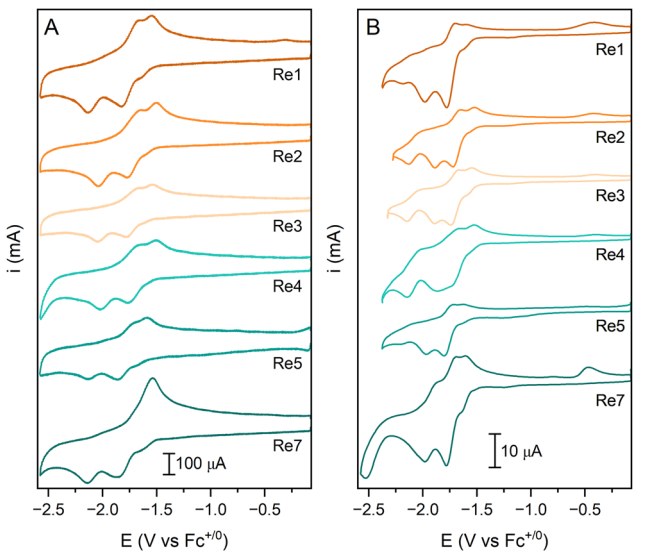

Fig. 6 Cyclic voltammograms of **Re1–5** and **Re7** recorded in acetonitrile under N_2 at scan rates (A) 10 V s^{-1} and (B) 0.1 V s^{-1} (supporting electrolyte 0.1 M *n*-Bu_4BF_4). **Re7** is shown for comparison.

Table 2 Reductive peak potentials at 10 V s^{-1} scan rates, and diffusion coefficients (*D*) of **Re1–5** and **Re7** from cyclic voltammetry in acetonitrile at varying scan rates (Fig. S27†)

Complex	$E^{(1)}_{1/2}$ (V)[a]	$E^{(2)}_{p}$ (V)[b]	D (cm^2 s^{-1})
Re1	−1.75	−2.13	9.87×10^{-6}
Re2	−1.70	−2.04	6.64×10^{-6}
Re3	−1.70	−2.04	5.61×10^{-6}
Re4	−1.69	−2.03	5.00×10^{-6}
Re5	−1.77	−2.13	2.67×10^{-6}
Re7	−1.73	−2.15	6.40×10^{-6}

[a] Mid-point potential for the 1st quasi-reversible reduction. [b] Peak potential for the irreversible 2nd reduction.

Under fast scan rate conditions (10 V s^{-1}, Fig. 6A), all Re complexes display two reduction waves: the first reduction is quasi-reversible, and the second is irreversible. The reduction potentials for the two processes at 10 V s^{-1} are listed in Table 2 ($E_{1/2}$ for the 1st reduction and peak potential (E_p) for the irreversible 2nd reduction). **Re2–4** exhibit the 1st reduction feature at ~−1.70 V and the 2nd irreversible reduction feature at ~−2.04 V. **Re1** and **Re5** display the first reduction feature at −1.75 V and −1.77 V, respectively, and the second reduction feature at −2.13 V. The slight anodic shift of the reduction potentials for **Re2–4** is rationalised by the electron-withdrawing nature of the phenyl substituent at the 4′-position of the tpy ligand. The more negative reduction potentials for **Re5** can be attributed to the electron donation from the ferrocene moiety (*vide infra*). Based on previous reports on Re(bpy)$(CO)_3$X-type complexes, the first reduction is attributed to a ligand (terpyridine)-centred process to form an anionic radical species, $[Re^{I}(tpy^{\bullet-})(CO)_3Br]^-$, that can undergo slow Br^- loss.[30,76] The second event is assigned to a metal-centred reduction to Re^0, leading to a rapid loss of Br^- and the formation of a 5-coordinate species, $[Re^0(tpy^{\bullet-})(CO)_3]^-$. This is consistent with the additional oxidation peak observed in the potential range −1.50 to −1.55 V during the return scan, which can be attributed to the oxidation of pentacoordinate species. Moreover, reversing the potential scan before the second reduction still resulted in the second reoxidation peak, which is in line with the quasi-reversibility of the first reduction process at scan rates >1 V s^{-1} due to the slow Br^- loss from $[Re^{I}(tpy^{\bullet-})(CO)_3Br]^-$ (Fig. S28†).

When the voltammograms were recorded at slower scan rates (0.1 V s^{-1}, Fig. 6B), a third irreversible reduction wave was observed for **Re1–5** at a more cathodic potential (~−2.15 V), suggesting the formation of new species on a longer time scale. This peak is more pronounced for **Re2–4** than **Re1** and **Re5**. We speculate that this reduction peak at <−2.15 V can be caused by Re–Re dimerisation, which has been reported previously in analogous bipyridine catalysts.[77] This is further supported by the small oxidation wave observed at ~−0.4 V during the return scan, which is assigned to the oxidation of a Re^0–Re^0 dimeric species.[78,79] The additional reduction and oxidation features disappear at a faster scan rate (>2 V s^{-1}; Fig. S28†), suggesting that the dimerisation step proceeds too slowly to be observed on the CV timescale. Interestingly, the first two reductions are well-separated for **Re2** and **Re3**, whereas those two peaks coalesced to a broad wave for **Re4** at 100 mV s^{-1}. For **Re5**, oxidation of the ferrocene unit appended to the terpyridine framework is observed at ~0.24 V, which indicates that the Fe-centre is significantly electron deficient compared with unmodified ferrocene, consistent with the more cathodic reduction potentials of **Re5**. Careful inspection of the oxidation wave suggests the presence of an overlapping irreversible peak which can be tentatively attributed to $Re^{I/II}$ oxidation.

The CVs of **Re1–5** and **Re7** at varying scan rates show that the reductive peak currents (i_p) vary linearly *versus* the square root of the scan rate (Fig. S27†), consistent with diffusion-

This journal is © The Royal Society of Chemistry 2023

Open Access Article. Published on 03 2566. Downloaded on 6/2/2569 0:03:00.
This article is licensed under a Creative Commons Attribution-NonCommercial 3.0 Unported Licence.

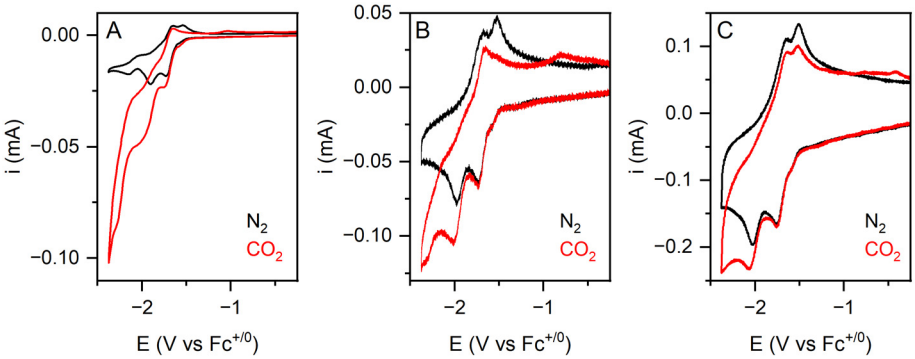

Fig. 7 Cyclic voltammograms of **Re2** recorded in acetonitrile under N_2 and CO_2 at different scan rates: (A) 0.1 V s^{-1}, (B) 2 V s^{-1} and (C) 10 V s^{-1} (supporting electrolyte 0.1 M *n*-Bu_4BF_4).

controlled homogeneous systems. The diffusion coefficients (D) for the **Re1–5** are comparable to that determined for **Re7** and those reported for analogous Re-complexes.[41] The decrease in D values within the **Re1–5** series is approximately in line with the steric bulk of the terpyridine ligand.

Electrocatalytic CO_2 reduction

Following the studies under N_2, cyclic voltammetry was performed in a CO_2-saturated electrolyte to evaluate the catalytic activity of **Re1–5** relative to **Re7** for CO_2 reduction. All complexes display current enhancement under CO_2 at either the same or a more negative potential than their second reduction features, demonstrating electrocatalytic CO_2 reduction. The catalytic response of **Re2** under CO_2-saturated conditions at different scan rates is shown in Fig. 7. Catalytic voltammograms for **Re1**, **Re3–5** and **Re7** are included in the ESI (Fig. S29 and S30†). As shown in Fig. 7, the first reduction process remains largely unaffected by the presence of CO_2 and its quasi-reversibility is maintained at the scan rates investigated here (25–0.1 V s^{-1}) (Fig. S30†). This is consistent with the hypothesis that the singly reduced Re species undergoes slow Br^- loss to form the 5-coordinate species (too slow for the CV timescale), which is necessary for CO_2 binding and activation at the Re centre. Interestingly, the 2nd oxidation peak at ~−1.55 V during the return scan disappears at scan rates ≤2 V s^{-1}, indicating that the doubly reduced species is consumed *via* a reaction with CO_2 at slower scan rates (Fig. 7B). Higher scan rates (>2 V s^{-1}) do not allow sufficient time for catalyst turnover, which provides a qualitative measure of the timescale of turnover frequency for **Re2**. Under faster scans (10 V s^{-1}, Fig. 7C), **Re2** exhibits a relatively modest current enhancement at the 2nd reduction feature. Similar responses are observed for the other Re catalysts under CO_2 at different scan rates (Fig. S30†).

The catalytic voltammograms under CO_2 and N_2 were analysed to compare the activity of the Re complexes. The ratio of the peak current in the presence of CO_2 (i_{cat}) and the corresponding reductive peak in the absence of a substrate (i_p) serves as a useful measure to assess and compare the activity of different Re complexes.[80] These i_{cat}/i_p ratios at a 0.1 V s^{-1} scan rate and the corresponding half-wave potentials for electrocatalytic CO_2 reduction by the Re complexes are summarised in Table 3. The catalytic currents (i_{cat}) were determined from the plateau shape of the catalytic response in the CVs at strongly reducing potentials (<−2.15 V) (Fig. S31†). **Re1–5** and **Re7** display i_{cat}/i_p ratios in the range of 7.1–9.6, which suggests that the rate of CO_2 electroreduction is similar for these complexes, with **Re4** exhibiting the largest enhancement and **Re2** exhibiting the lowest. It should be noted that the i_{cat}/i_p value only serves as a proxy for the catalytic rate, and there is a degree of error inherent in the values reported here due to the nature of overlapping catalytic waves at different potentials. During catalysis in the pure kinetic regime (CO_2 concentration at the electrode surface is equal to the bulk concentration), the normalised peak catalytic current (i_{cat}/i_p) can be used to derive the pseudo-first-order catalytic rate constant (k_{obs}).[80,81] However, the prerequisites for applying this method are the scan-rate independent catalytic current plateau and 'S-shaped' catalytic waves, which are not observed for the Re complexes investigated here. The catalytic currents for all complexes display a scan-rate dependence up to 25 V s^{-1}, precluding the derivation of k_{obs} from i_{cat}/i_p. An alternative method to estimate k_{obs} from CVs without 'S-shaped' catalytic waves is to apply 'foot-of-the-wave analysis' (FOWA), developed by Savéant and Costentin.[81,82] However, FOWA requires an accessible 'foot' to the catalytic wave (*i.e.*, the absence of redox processes distorting the foot of the wave). This is not applicable for the Re catalysts because the two reduction events overlap at the foot of the catalytic wave, and the onset occurs at a more cathodic potential than the 2nd reduction. Due to the lack of reliable methods for estimating k_{obs}, the discussion on comparing the catalytic rate for Re complexes has been restricted to the difference in i_{cat}/i_p.

Previous reports on Re(bpy)$(CO)_3$X (X = Cl, Br) catalysts have suggested that CO_2 reduction can proceed *via* two pathways: (1) a slow 1e$^-$ pathway that occurs after the 1st ligand-centred reduction and (2) a faster 2e$^-$ pathway that is activated after the 2nd metal-centred reduction and subsequent rapid loss of X^-.[77] This is consistent with the CV data for Re-complexes recorded at various scan rates, which show a minimal current

Open Access Article. Published on 03 2566. Downloaded on 6/2/2569 0:03:00.
This article is licensed under a Creative Commons Attribution-NonCommercial 3.0 Unported Licence.

Table 3 Catalytic parameters for **Re1–5** and **Re7** derived from cyclic voltammetry in neat acetonitrile and controlled potential electrolyses in a CO_2-saturated acetonitrile/water (0.5% v/v) mixture

Catalyst	E_{cat} (V *vs.* $Fc^{+/0}$)[a] (at 0.1 V s^{-1})	i_{cat}/i_p [a] (at 0.1 V s^{-1})	E_{app} [b] (V *vs.* $Fc^{+/0}$)	CO[b] (μmol)	FY_{CO} [b]	TON_{CO} [b]
Re1	−2.32	8.9	−2.1	3.2	88%	2.1
			−2.3	5.0	98%	3.3
Re2	−2.20	7.1	−2.1	4.1	87%	2.7
			−2.3	3.5	78%	2.3
Re3	−2.21	8.7	−2.3	3.1	94%	2.1
Re4	−2.14	9.6	−2.1	0.9	62%	0.6
			−2.3	1.8	70%	1.2
Re5	−2.31	9.0	−2.1	2.3	85%	1.5
			−2.3	2.8	92%	1.9
Re7 [c]	−2.42	8.1	—	—	—	—

[a] E_{cat} (half-wave potential for the catalytic wave) and i_{cat}/i_p values were determined from CVs recorded in acetonitrile. [b] E_{app} (applied potential), amount of CO, Faradaic yields (FY_{CO}) and catalyst turnover numbers (TON_{CO}) were determined from 3.0 min CPE performed in CO_2-saturated electrolyte using a glassy carbon plate working electrode. [c] CPE was not performed with **Re7**.

increase at the 1st reduction step (ν = 0.1–25 V s^{-1}). Significant current enhancement is only observed at further cathodic potentials than the 2nd reduction step and relatively slower scan rates (<1 V s^{-1}) (Fig. 7B and S32†).

Electrocatalytic CO_2 reduction in the presence of proton sources

The influence of a proton source on electrocatalysis was evaluated using **Re2** as the catalyst in the presence of water, trifluoroethanol (TFE), and acetic acid in a CO_2-saturated acetonitrile electrolyte.[35] Since an acidic environment can modulate the CO_2 reduction activity on the electrode surface,[83] we chose to evaluate three proton sources *via* cyclic voltammetry with increasing acidity: water (pK_a^{aq} 15.7) < trifluoroethanol (pK_a^{aq} 12.5) < acetic acid (pK_a^{aq} 4.7). In the presence of water, the hydration of CO_2 forms H_2CO_3, which acts as a proton source with a pK_a of 17.03 in acetonitrile. As discussed above, the quasi-reversibility of the 1st reduction is retained under CO_2, but the second oxidation peak at −1.52 V in the return scan disappeared (Fig. 8A). Upon the incremental addition of water, a slight increase in current at −1.72 V was observed with a concomitant drop in current at −1.95 V and a gradual loss of reversibility of the 1st reduction. The variations in i_{cat}/i_p at the two reduction steps are shown in the inset of Fig. 8A. It has been postulated that the $1e^-$ pathway leads to a reductive disproportionation of CO_2 to form CO and CO_3^{2-}. We speculate that at higher proton concentrations, the pendant pyridine near the Re centre potentially facilitates CO_3^{2-} release by forming a network of hydrogen-bonded water molecules.[17] However, it should be noted that a pendant pyridine group has a $pK_a \sim 5$ (estimated based upon the pK_a of pyridinium cations in aqueous solution[84]), and it is not expected to undergo direct protonation by H_2CO_3. Overall, the voltammograms suggest that adding water provides a minimal improvement in the

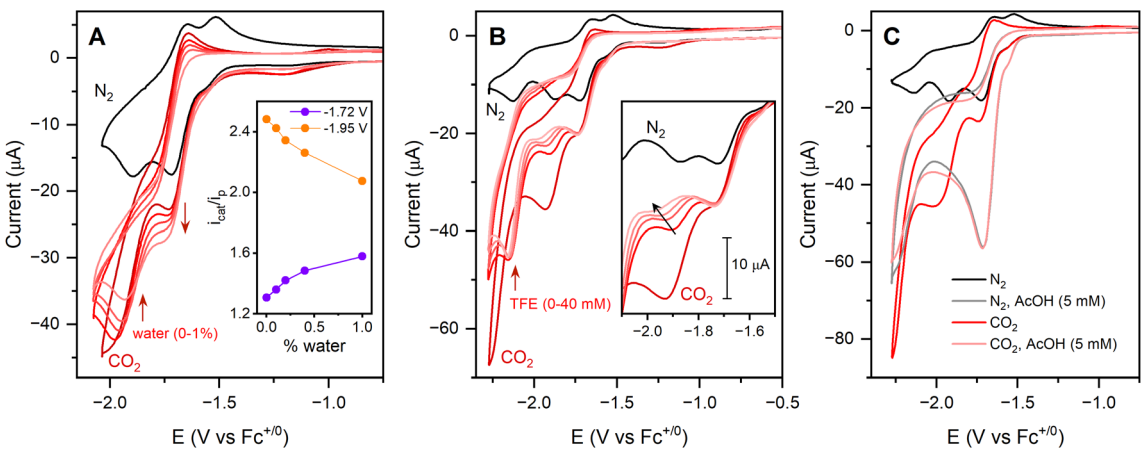

Fig. 8 Catalytic CVs of **Re2** (1 mM) in CO_2-saturated acetonitrile containing three different proton sources: (A) CVs in the presence of increasing amount of water (0%, 0.1%, 0.2%, 0.4%, and 1%; v/v). The red trace presents 0% water and current traces with increasing water content is shown by the faded red traces. The inset figure shows the i_{cat}/i_p ratio variation with water content at the two reduction steps. (B) CVs in the presnce of trifluoroethanol (0, 10, 20, 30, and 40 mM with the red trace presenting 0% water) The inset figure shows the shift of the peak potential of the second reduction step with incremental addition of TFE. (C) CVs under N_2 and CO_2 in the presence and absence of acetic acid (5 mM). All voltammograms were recorded at a 100 mV s^{-1} scan rate in 0.1 M *n*-Bu_4BF_4 supporting electrolyte.

This journal is © The Royal Society of Chemistry 2023

Open Access Article. Published on 03 2566. Downloaded on 6/2/2569 0:03:00.
This article is licensed under a Creative Commons Attribution-NonCommercial 3.0 Unported Licence.

catalytic activity. A similar effect of water was observed for other Re complexes (Fig. S33†).

As shown in Fig. 8B, upon addition of TFE to a CO_2-saturated solution of **Re2**, the voltammograms show no change in the reductive peak current at the 1st reduction (−1.73 V) and a significant decrease in the peak current at the 2nd reduction (−1.92 V). In the presence of TFE, the large catalytic wave at ∼−2.25 V displayed a decrease in current and shifted slightly to a more positive potential, forming a well-defined peak at −2.15 V. While increasing the concentration of TFE did not lead to any further increase in peak current at −2.15 V, the 2nd reduction feature (∼−1.92 V) underwent an incremental cathodic shift coupled with a gradual decrease of the peak current (Fig. 8B inset). This suggests that TFE is not directly involved in the rate-limiting step. At 50 mM TFE concentration, the 2nd reduction feature shifted to ∼−2.02 V and it was barely discernible (Fig. S34†). This can be tentatively described as the 'EC' step, where TFE reacts with the singly reduced species ('C' step), leading to its depletion at the electrode surface and a subsequent cathodic shift of the 2nd reduction. When the CVs were recorded at a faster scan rate (10 V s^{-1}), the first two reduction peaks displayed minimal current enhancement in the presence of TFE, but a new reduction wave appeared at ∼−2.3 V with a concomitant loss of the reoxidation peak at −1.52 V (Fig. 9). Upon purging the electrolyte with N_2, the peak current at −2.3 V was nearly halved, and the peak current at ∼−2.04 V (the 2nd reduction step) decreased to the pre-CO_2 level (black and grey trace, Fig. 9). This suggests that the reduction wave at −2.3 V and the modest current enhancement at −2.04 V can be attributed to electrocatalytic CO_2 reduction. Notably, there is a non-trivial contribution from proton reduction at −2.3 V as shown by the reduction wave under N_2 (grey trace). Since this peak is only observed in the presence of TFE, we can speculate that it originates from the protonation of the doubly reduced species.

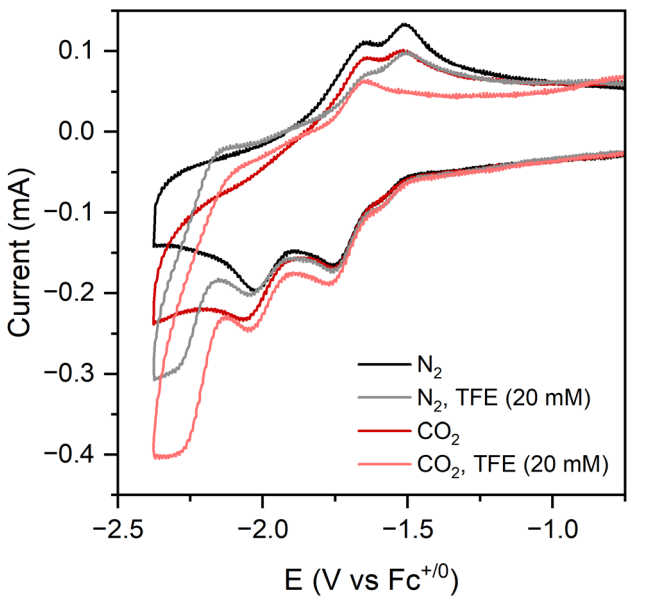

Fig. 9 CVs of **Re2** (1 mM) in N_2 or CO_2-saturated acetonitrile containing varying amounts of TFE (0 or 20 mM). Voltammograms were recorded at a 10 V s^{-1} scan rate in 0.1 M n-Bu_4BF_4 supporting electrolyte.

Interestingly, the reoxidation peak at −1.52 V reappeared when scanned under N_2 (grey trace, Fig. 9), suggesting that the pentacoordinate species is regenerated. At a 100 mV s^{-1} scan rate (Fig. 8B), all three reduction steps display a current increase, which indicates that CO_2 reduction can be observed for singly and doubly reduced species on slower CV timescales. For realising the catalysis in kinetic regimes and to achieve 'S-shaped' catalytic waves under CO_2/TFE, the scan rate was increased up to 25 V s^{-1}, but the plateau current kept increasing with the scan rate, which excluded the possibility of determining k_{obs} (Fig. S35†) (higher scan rates were not measured due to instrument limitations).

Finally, acetic acid was evaluated as a proton source for CO_2 due to its lower pK_a, which allows protonation of the pendant pyridine. As shown in Fig. 8C, the CVs recorded in the presence of 5 mM AcOH under N_2 and CO_2 are nearly identical, suggesting that CO_2 reduction is hindered under acidic conditions. Adding acetic acid renders the 1st reduction event irreversible, along with a ∼4-fold increase in the peak current (E_p = −1.70 V). However, no further increase in peak current was observed upon increasing the acetic acid concentration from 5 mM to 10 mM, suggesting that it is not a catalytic wave. We speculate that the protonation of the terpyridine ligand causes this proton-responsive behaviour, and the irreversible reduction is tentatively assigned to the multi-electron reduction of the protonated complex.

Controlled potential electrolysis

The catalytic performance of the compounds was investigated by 30 min controlled potential electrolysis (CPE) at −2.1 V and −2.3 V (*vs.* $Fc^{+/0}$) in CO_2-saturated acetonitrile containing 0.5% water (v/v) as the proton source. TFE was avoided as the proton source to minimise the competing proton reduction. The applied potentials correspond to overpotentials of 0.75 V and 0.95 V, respectively, for CO_2 reduction to CO $\left(E^0_{CO_2/CO} = -1.35\,V \text{ in acetonitrile}\right)$.[73] After CPE, the headspace of the electrochemical cell was analysed by gas chromatography (GC), and the electrolyte was analysed by ion chromatography and ^{1}H NMR spectroscopy for other liquid products (formic acid, methanol). CO was detected as the only CO_2-reduction product from electrolysis. No H_2 was detected for any Re catalysts. During electrolysis, the current density slowly decayed (Fig. S36†). This suggests slow catalyst decomposition, consistent with the change of colour of the electrolyte from bright yellow to pale brown. This is supported by the post-electrolysis characterisation of the electrolyte with UV-Vis (Fig. S37–S39†). To confirm that the molecular Re-complexes catalyse CO_2-to-CO conversion in solution, a rinse test was performed with the post-electrolysis glassy carbon electrode under identical conditions for **Re3** (Fig. S40†). The rinsed electrode showed negligible current with no CO_2R activity, supporting the homogenous nature of the CO_2R catalysis. No CO

Open Access Article. Published on 03 2566. Downloaded on 6/2/2569 0:03:00.
This article is licensed under a Creative Commons Attribution-NonCommercial 3.0 Unported Licence.

was detected in the control experiments performed under N_2 or without a catalyst.

The electrolysis results are summarised in Table 3. All Re complexes, except **Re4**, produced CO with a high FY_{CO} (>85%) after 30 min electrolysis. In contrast, the FY_{CO} after electrolysis with **Re4** was 62% and 70% at −2.1 V and −2.3 V, which could be attributed to the lower stability of the complex under reductive conditions. This is consistent with the fast decay of current density observed during electrolysis with Re4. Total catalytic turnover numbers for CO (TON_{CO}) were determined from the amount of CO produced after 30 min electrolysis. The TON_{CO} values were in the range of 1.2–3.3, with **Re1** displaying the best activity at −2.3 V. Overall, the performance of the catalysts under electrolysis conditions does not vary significantly within the series. Interestingly, applying a more reductive potential during electrolysis (−2.1 V *versus* −2.3 V) had a minimal influence on FY_{CO} and TON_{CO}. Electrolysis at −2.1 V is expected to follow the $2e^-$ pathway for **Re2**, **Re3**, and **Re4** (Table 3), whereas it would proceed *via* the $1e^-$ pathway for **Re1** and **Re5** as the second metal-centred reduction occurs at a more negative potential for the latter two complexes (~−2.3 V, Table 3). This is consistent with the slightly improved CO yield, and the TON_{CO} observed for electrolysis at −2.3 V for **Re1** and **Re5**.

Spectroelectrochemistry of Re5

A distinct colour change was observed for **Re5** before and after the electrolysis experiments, which prompted us to investigate **Re5** using UV-Vis spectroelectrochemistry in acetonitrile. The UV-Vis spectra of **Re5** at reducing potentials are shown in Fig. 10. At an open circuit voltage, the starting solution of **Re5** displays a peak at 516 nm in the visible region. Upon reduction, a new absorbance appears at ~580 nm at <−1.9 V (*vs.* $Fc^{+/0}$) and shows complete conversion at about −2.3 V. The final UV-Vis spectrum also shows a broad absorbance in the 400–500 nm range. The CV of **Re5** suggests that this is likely to be a $2e^-$ reduced species. Interestingly, the UV-Vis spectra show very little change after the first reduction at −1.75 V (Fig. S36†).

TDDFT data suggest that the 516 nm absorbance majorly corresponds to a d–d transition within the ferrocenyl moiety in the ligand. We speculate that the extra electron density in the reduced **Re5** species (at <−2.1 V) is partly delocalised on the ferrocenyl moiety through the coordinating terpyridine unit. Unfortunately, we were unable to isolate the reduced species for further characterisation. The spectroelectrochemical measurements show the evolution of a new peak at 590 nm in the ground state absorption spectrum under higher applied potentials. This wavelength is the same region where a delayed stimulated emission is observed in our measurements. It is difficult to predict if the bands at 590 nm in the TA and spectroelectrochemistry originate from the same state. Currently, detailed transient spectro-electrochemical measurements are carried out to ascertain 590 nm bands for **Re5**. If these bands correspond to the same state, then the same molecule could be used as an electrochemical and photochemical catalyst for fixing atmospheric CO_2.

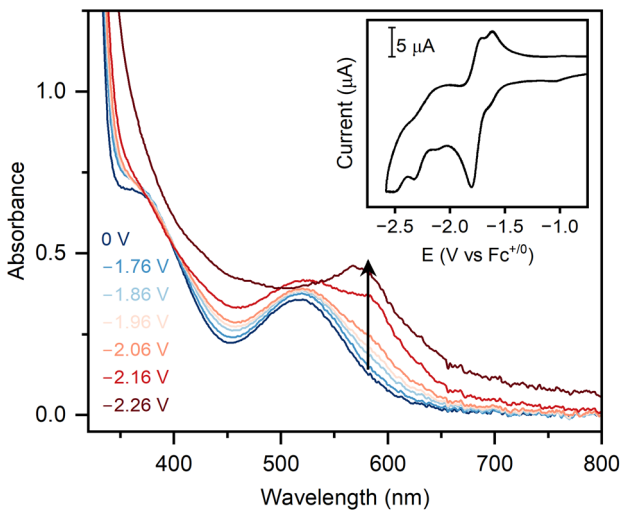

Fig. 10 UV–Vis spectroelectrochemical data for **Re5** (1 mM), showing the steady-state relative absorbance at different applied potentials under N_2. The inset figure shows the cyclic voltammogram of **Re5** at the reductive potential.

Conclusions

A series of Re(I)(**L**)$(CO)_3$Br complexes containing 4′-substituted-2,2′:6′,2″-terpyridine ligands (**L2–5**) were synthesised and characterised (**Re2–5**). Analytical data suggest that the tpy ligand coordinates to the Re centre in κ^2-NN mode with all CO ligands in the *cis* position. TAS and TDDFT studies indicate that a highly intense band around 303–310 nm is a combination of π(tpy)–π*(tpy) and π_{yz}(Re–Br)–π*(tpy), categorising them to ILCT and MLCT bands for all complexes. According to the TDDFT calculation, another MLCT band is observed around 430 nm for **Re1–4** due to the $5d_{yz}$(Re)–π*(tpy) transition. Interestingly, for **Re5**, the second MLCT band also involves the $3d_{xy}$ orbitals of the iron centre in the ferrocene substituent along with the $5d_{yz}$(Re)–π*(tpy) transition. **Re5** also showed a d–d transition around 516 nm owing to a ferrocenyl moiety probed by *in situ* spectroelectrochemistry. An additional excited state was observed for the **Re5** complex in transient absorption spectroscopy due to the presence of the ferrocenyl moiety. The electrochemical data demonstrate the influence of the substitution on the tpy ligand on the redox property of the complexes. The catalytic activity of all Re complexes towards CO_2-to-CO electroreduction in acetonitrile is demonstrated using cyclic voltammetry and controlled potential electrolysis, which reveal comparable catalytic currents for tpy-substituted Re-complexes (**Re1–5**) and the bipyridine analogue (**Re7**). Within the series, the best activity towards CO_2 reduction is observed for **Re4** based on the i_{cat}/i_p ratios determined from cyclic voltammetry, and the best TON_{CO} and FY_{CO} were obtained for **Re1** using controlled potential electrolysis. The electrocatalysis was mostly unaffected by adding water

This journal is © The Royal Society of Chemistry 2023

Open Access Article. Published on 03 2566. Downloaded on 6/2/2569 0:03:00.
This article is licensed under a Creative Commons Attribution-NonCommercial 3.0 Unported Licence.

(Brønsted acid), suggesting that the pendant pyridine group does not directly engage in CO_2 reduction under weakly acidic conditions. However, the electrocatalytic activity of the complexes can be modulated by using proton sources with lower pK_a (TFE and AcOH), as demonstrated by the voltametric data recorded here. In summary, this work expands the library of Lehn-type Re-catalysts for CO_2 reduction and demonstrates the effect of integrating terpyridine ligands with an uncoordinated pyridine towards electrocatalytic CO_2 conversion.

Experimental section

Materials

Ethanol was received from LabChem; toluene and diethyl ether were received from SRL Chemicals. Ethanol and diethyl ether were used as received, and toluene was dried over sodium before use. For the cyclic voltammetric measurements, acetonitrile was dried over phosphorous pentoxide, and dried DMF was used as obtained from SRL Pvt. Ltd. Rhenium pentacarbonyl bromide, $Re(CO)_5Br$, was purchased from Sigma Aldrich, aldehydes from Spectrochem Pvt. Ltd, potassium hydroxide from Avra Synthesis Pvt. Ltd, and aqueous ammonia from Qualigen Laboratories. All reagents were used without further purification. The ligand **L1** was obtained from BLD Pharmatech (India) Pvt. Ltd through Carbanio. All metal complex synthesis reactions were carried out using the Schlenk technique. The filtration and other manipulations were done in the open air.

Instrumentation

Melting points of the ligands were recorded using the DBK-programmable melting point (max = 320 °C) apparatus. ^{1}H and $^{13}C\{^1H\}$ NMR spectra were acquired on a Bruker AVANCE III HD spectrometer using 500 MHz (^{1}H NMR) or a Bruker ASCEND™ spectrometer using 400 MHz (^{1}H NMR) in $CDCl_3$ (δ = 7.26 ppm); DMSO-d_6 (δ = 2.50 ppm) or 125 MHz or 101 MHz ($^{13}C\{^1H\}$ NMR) in $CDCl_3$ (δ = 77.1 ppm); and DMSO-d_6 (δ = 39.5 ppm) at 298 K. Multiplicities of the signals are reported using the following abbreviations: s, singlet; d, doublet; dd, doublet of doublet; t, triplet; dt, doublet of triplet; m, multiplet; br, broad. The UV-Vis absorption spectral measurements of ligands and complexes in DMF or acetonitrile solution were performed with a JASCO – V-770 UV-Visible/NIR double-beam spectrophotometer. In the ATR mode, the infrared (IR) spectra were recorded using a Shimadzu IRAffinity-1S spectrophotometer (40 scans, scanned in 4000–400 cm^{-1}, resolution 4 cm^{-1}). The reverse phase HPLC method was carried out on a C18 column (100 mm × 2.1 mm i.d., 3 μm), maintained at 40 °C, using aqueous acetonitrile gradients containing 1% ammounium formate as the mobile phase with a flow rate of 0.2 mL min^{-1}. A photodiode array (PDA) detector set at 254 nm was used, unless stated otherwise. Elemental analysis was performed using an Elementar Vario Macro cube organic chemical analyser (BITS Goa). Elemental analysis for **Re5** was done at Mikrolab Kolbe, Oberhausen, Germany. MS were recorded using a Bruker Daltonics – micrOTOF-Q II – ESI-Qq-TOF mass spectrometer (IISER Bhopal) or Shimadzu LCMS – 2020 with ESI ionisation mode.

Synthesis and characterisation of ligands

In a Schlenk flask with a magnetic stirbar, aldehyde (1.0 equiv.) was dissolved in 5.0 mL of EtOH at room temperature. To this solution, 2-acetylpyridine (2.0 equiv.) was added and stirred to complete the dissolution. KOH pellets (2.0 equiv.) and aq. NH_3 (60%, 50 equiv.) were added to the solution. The mixture was refluxed at 70 °C for 12 h. The clear orange-coloured solution changes to a turbid mixture during the reaction, indicating the desired product formation. After cooling the solution to room temperature, it is kept at 4 °C overnight, which helps to form more precipitate. The white or off-white solid was collected by filtration, washed with cold EtOH (3 × 10 mL), and air-dried for 24 h.

4′-Phenyl-2,2′:6′,2″-terpyridine (L2). 30% yield (82.8 mg, 0.268 mmol). M.P.: 196 °C (lit. report: 202–204 °C).[85] ^{1}H NMR ($CDCl_3$, 500 MHz) δ (ppm): 8.75 (s, 2H), 8.73 (d, 2H, J = 4.49 Hz), 8.66 (d, 2H, J = 7.95 Hz), 7.91 (d, 2H, J = 7.46 Hz), 7.87 (td, 2H, J = 7.95, 1.62 Hz), 7.51 (t, 2H, J = 7.46 Hz), 7.45 (t, 1H, J = 7.32 Hz), 7.34 (dd, 2H, J = 4.99, 1.62 Hz). $^{13}C\{^1H\}$ NMR ($CDCl_3$, 125 MHz) δ (ppm): 156.3, 155.9, 150.4, 149.2, 138.5, 136.9, 129.0, 128.9, 127.4, 123.8, 121.4, 118.9. ATR-IR (cm^{-1}): 3047, 3008, 1599, 1582, 1543, 1471, 1394, 1267, 1038, 889, 757. UV–Vis {λ_{max}/nm (10^3 ε/L mol^{-1} cm^{-1})}: in acetonitrile: 252 (23.0), 275 (22.5), 329 (1.8); in DMF: 309 (25.3). RP-HPLC: 3.424 min (mobile phase: acetonitrile and 1% ammonium formate in water) 95 : 5 (v/v). ESI-MS (m/z): 310 (expected 310 (M + H^+), $C_{21}H_{16}N_3^+$) and 332 (expected 332, (M + Na^+), $C_{21}H_{15}N_3Na^+$).

4′-(4-Methylphenyl)-2,2′:6′,2″-terpyridine (L3). 40% yield (217 mg, 0.671 mmol). M.P.: 165 °C (lit. report: 168 °C).[86] ^{1}H NMR ($CDCl_3$, 500 MHz) δ (ppm): 8.73 (s, 2H), 8.72 (d, 2H, merged with the singlet), 8.66 (dt, 2H, J = 7.90, 1.10 Hz), 7.85 (td, 2H, J = 7.92, 1.62 Hz), 7.82 (d, 2H, J = 8.10 Hz), 7.34–7.30 (m, 4H), 2.42 (s, 3H). $^{13}C\{^1H\}$ NMR ($CDCl_3$, 125 MHz) δ (ppm): 156.4, 155.9, 150.2, 149.1, 139.1, 136.8, 135.5, 129.7, 127.2, 123.8, 121.4, 118.6, 21.3. ATR-IR (cm^{-1}): 3051, 3013, 1603, 1585, 1567, 1510, 1467, 1386, 1038, 825, 783, 732. UV–Vis {λ_{max}/nm (10^3 ε/L mol^{-1} cm^{-1})}: in acetonitrile: 253 (28.0), 278 (31.1), 332(1.5); in DMF: 278 (25.3), 316 (10.2). RP-HPLC: 3.950 min (acetonitrile and 1% ammonium formate in water) 95 : 5 (v/v). ESI-MS (m/z): 324 (expected 324 (M + H^+), $C_{22}H_{18}N_3^+$) and 346 (expected 346, (M + Na^+), $C_{22}H_{17}N_3Na^+$).

4′-(4-Bromophenyl)-2,2′:6′,2″-terpyridine (L4). 48% yield (310 mg, 0.798 mmol). M.P.: 126 °C (lit. report: 125 °C).[87] ^{1}H NMR ($CDCl_3$, 500 MHz) δ (ppm): 8.72 (d, 2H, J = 4.90 Hz), 8.69 (s, 2H), 8.65 (d, 2H, J = 7.95 Hz), 7.87 (td, 2H, J = 7.67, 1.83 Hz), 7.76 (dt, 2H, J = 8.50, 1.83 Hz), 7.63 (dt, 2H, J = 8.54, 1.95 Hz), 7.35 (ddd, 2H, J = 4.76, 2.73, 1.08 Hz). $^{13}C\{^1H\}$ NMR ($CDCl_3$, 125 MHz) δ (ppm): 156.1, 156.0, 149.1, 149.0, 137.4, 136.9, 132.1, 128.9, 124.0, 123.5, 121.4, 118.6. ATR-IR (cm^{-1}): 3052, 3014, 1605, 1586, 1562, 1541, 1462, 1443, 1376, 1261, 1074, 788, 735. UV–Vis {λ_{max}/nm (10^3 ε/L mol^{-1} cm^{-1})}: in acetonitrile: 253 (28.1), 276 (30.8), 330(2.5); in DMF: 275 (32.3),

Open Access Article. Published on 03 2566. Downloaded on 6/2/2569 0:03:00.
This article is licensed under a Creative Commons Attribution-NonCommercial 3.0 Unported Licence.

312 (7.36). RP-HPLC: 4.502 min (acetonitrile and 1% ammonium formate in water) 95 : 5 (v/v). ESI-MS (*m*/*z*): 388 (expected 388, $(M + H^+)$, $C_{21}H_{15}BrN_3^+$).

4′-(2-Ferrocenyl)-2,2′:6′,2′-terpyridine (L5). 83% yield (310 mg, 0.741 mmol). MP: 179 °C with blackening (lit. report: 310 °C, decomposition).[88] ^{1}H NMR ($CDCl_3$, 500 MHz) δ (ppm): 8.75 (d, 2H, J = 2.65 Hz), 8.65 (d, 2H, J = 7.75 Hz), 8.53 (s, 2H), 7.86 (t, 2H, J = 7.56 Hz), 7.35 (t, 2H, J = 6.10 Hz), 5.02 (s, 2H), 4.47 (s, 2H), 4.10 (s, 5H). $^{13}C\{^1H\}$ NMR ($CDCl_3$, 125 MHz) δ (ppm): 156.5, 155.3, 150.8, 149.1, 136.8, 123.7, 121.4, 117.7, 81.6, 70.2, 70.0, 67.4. ATR-IR (cm^{-1}): 3094, 3077, 2981, 1610, 1586, 1568, 1548, 1462, 1404, 1270, 1098, 1022, 788, 725. UV–Vis {λ_{max}/nm (10^3 ε/L mol^{-1} cm^{-1})}: in acetonitrile: 250 (17.1), 280 (17.8), 365 (0.83), 460 (0.26); in DMF: 283 (17.9), 363 (1.29), 459 (0.56). RP-HPLC: 4.389 min (acetonitrile and 1% ammonium formate in water) 95 : 5 (v/v). ESI-MS (*m*/*z*): 418 (expected 418, $(M + H^+)$, $C_{25}H_{20}FeN_3^+$) and 440 (expected 440, $(M + Na^+)$, $C_{25}H_{19}FeN_3Na^+$).

Synthesis and characterisation of Re(I) complexes

The Re(I) complexes were synthesised following modified literature procedures: **Re1**,[89] **Re2**,[61] **Re3**[90] (Cl variation), and **Re4**[91] (Cl variation). A Schlenk flask equipped with a magnetic stirbar was charged with ligand (1.0 equiv.) and dissolved in 3 mL of dry toluene under argon. To this solution, $Re(CO)_5Br$ (1.0 equiv.) was added, and the reaction mixture was refluxed at 100 °C, wherein the colour changes from colourless to a yellow to dark orange solution for **Re1** to **Re4**. For **Re5**, the colour of the solution changed from brown to red. After the colour change was observed, it was stirred for more time and then cooled down to room temperature, leading to a precipitate, except for **Re5**. The solution was then decanted, and the precipitate was washed with toluene (2 × 5 mL), and then cold diethyl ether (2 × 5 mL). The compound was dried under vacuum at 340 mbar for 20 minutes.

Re1. In a Schlenk flask, terpyridine (29.3 mg, 0.123 mmol) and $Re(CO)_5Br$ (50.0 mg, 0.123 mmol) in toluene were refluxed for an hour, wherein the solution changed colour from colourless to yellow to slight orange. After filtration and vacuum drying, a yellow-coloured powder was obtained with 56% yield (40.0 mg, 0.068 mmol). MP: 275 °C with decomposition (lit. report: 278–280 °C).[92] ^{1}H NMR ($CDCl_3$, 400 MHz) δ (ppm): 9.14 (d, 1H, J = 5.09 Hz), 8.84 (d, 1H, J = 4.83 Hz), 8.27 (t, 2H, J = 8.32 Hz), 8.16 (t, 1H, J = 7.72 Hz), 8.10 (t, 1H, J = 7.72 Hz), 7.93 (t, 2H, J = 7.72 Hz, merged with the other signal), 7.90 (t, 1H, J = 7.72 Hz, 1H, merged with the other signal), 7.77 (d, 1H, J = 8.31 Hz), 7.53 (dd, 2H, J = 8.31, 5.94 Hz). ^{1}H NMR (DMSO-d_6, 400 MHz) δ (ppm): 9.07 (d, 1H, J = 4.8 Hz), 8.84 (t, 2H, J = 7.6 Hz), 8.78 (d, 1H, J = 4.1 Hz), 8.43 (t, 1H, J = 7.9 Hz), 8.36 (t, 1H, J = 7.4 Hz), 8.04 (t, 1H, J = 7.0 Hz), 7.89 (d, 1H, J = 7.5 Hz), 7.78 (dd, 2H, J = 21.5 Hz, J = 8.4 Hz,), 7.61 (q, 1H, J = 3.9 Hz). $^{13}C\{^1H\}$ NMR (DMSO-d_6, 101 MHz) δ (ppm): 197.3 (CO), 193.8 (CO), 190.2 (CO), 161.2, 157.8, 156.5, 156.2, 152.8, 149.3, 140.4, 140.0, 136.9, 127.7, 127.4 124.9, 123.7. ATR-IR (ν_{CO}/cm^{-1}): 2019, 1911, 1884. UV–Vis {λ_{max}/nm (10^3 ε/L mol^{-1} cm^{-1})}: in acetonitrile: 247 (21.5), 310 (15.5), 372 (2.80); in DMF: 309 (20.9), 375 (5.58). HRMS (*m*/*z*): calcd for $[M + Na^+]$ 605.9416, found $[M + Na^+]$ 605.9405. Anal calcd (in %) for $C_{18}H_{11}BrN_3O_3Re{\cdot}H_2O$: C, 35.95; H, 2.18; N, 6.99. Found: C, 35.35; H, 1.38; N, 6.88.

Re2. In a Schlenk flask, **L2** (39.0 mg, 0.125 mmol) and $Re(CO)_5Br$ (50.0 mg, 0.123 mmol) were dissolved in toluene and refluxed for 4 h, wherein the solution changed colour from colourless to slightly orange. After filtration and vacuum drying, a bright, yellow-coloured powder was obtained with 78% yield (63.0 mg, 0.096 mmol). MP: 270 °C with decomposition (lit. report: 265 °C).[61] ^{1}H NMR ($CDCl_3$, 500 MHz) δ (ppm): 9.13 (d, 1H, J = 4.97 Hz), 8.84 (d, 1H, J = 5.13 Hz), 8.27 (t, 2H, J = 8.98 Hz), 8.19–8.12 (m, 1H), 8.08 (t, 2H, J = 7.90 Hz), 7.92 (dd, 1H, J = 8.32, 7.36 Hz, merged with another signal), 7.90 (t, 1H, J = 7.53 Hz, merged with another signal), 7.76 (d, 1H, J = 7.90 Hz), 7.52 (dd, 1H, J = 7.88, 4.96 Hz), 7.27 (m, 2H, merged with solvent peak). ^{1}H NMR (DMSO-d_6, 400 MHz) δ (ppm): 9.09 (bs, 2H), 8.80 (d, 1H, J = 4.0 Hz), 8.37 (t, 1H, J = 7.6 Hz), 8.18 (bs, 3H), 8.06 (t, 1H, J = 7.1 Hz), 7.89 (d, 1H, J = 7.6 Hz), 7.78 (t, 1H, J = 5.9 Hz), 7.62 (br m, 5H). $^{13}C\{^1H\}$ NMR (DMSO-d_6, 101 MHz) δ (ppm): 197.5 (CO), 194.0 (CO), 190.5 (CO), 161.7, 158.0, 157.4, 156.4, 152.9, 150.7, 149.3, 140.0, 137.1, 134.8, 131.1, 129.5, 127.9, 127.6, 125.6, 125.1, 125.1, 124.5, 120.7. ATR-IR (ν_{CO}/cm^{-1}): 2013, 1908, 1878. UV–Vis {λ_{max}/nm (10^3 ε/L mol^{-1} cm^{-1})}: in acetonitrile: 266 (47.6), 380 (7.08); in DMF: 384 (9.27). ESI-MS (*m*/*z*): 660 (expected 659, $(M + H^+)$, $C_{24}H_{15}BrN_3O_3Re$). HRMS (*m*/*z*): calcd for $[M - CO + Na^+]$ 653.9775, found for $[M - CO + Na^+]$ 653.1380 and calcd for $[M - Br]^+$ 580.0643, found for $[M - Br]^+$ 580.0848. Anal calcd (in %) for $C_{24}H_{15}BrN_3O_3Re$: C, 43.71; H, 2.29; N, 6.38. Found: C, 43.02; H, 1.90; N, 6.24.

Re3. In a Schlenk flask, **L3** (39.8 mg, 0.123 mmol) and $Re(CO)_5Br$ (50.0 mg, 0.123 mmol) were dissolved in toluene and refluxed for 4 h, wherein the solution immediately changed colour to deep orange. After filtration and vacuum drying, a yellow-coloured powder was obtained with a 93% yield (77.0 mg, 0.114 mmol). M.P.: >300 °C. ^{1}H NMR ($CDCl_3$, 400 MHz) δ (ppm): 9.14 (d, 1H, J = 5.09 Hz), 8.83 (d, 1H, J = 4.83 Hz), 8.39 (d, 1H, J = 1.41 Hz), 8.34 (d, 1H, J = 8.03 Hz), 8.08 (td, 1H, J = 7.99, 1.16 Hz), 7.93 (d, 2H, J = 3.72 Hz), 7.90 (d, 1H, J = 1.31 Hz), 7.67 (d, 2H, J = 8.10 Hz), 7.52 (m, 2H), 7.36 (d, 2H, J = 7.09 Hz), 2.45 (s, 3H). ^{1}H NMR (DMSO-d_6, 400 MHz) δ (ppm): 9.11 (d, 1H, J = 7.1 Hz, merged with another signal), 9.08 (br s, 2H, merged with another signal), 8.80 (d, 1H, J = 4.1 Hz), 8.38 (t, 1H, J = 7.1 Hz), 8.15 (pseudo t, 3H, J = 8.8 Hz), 8.06 (t, 1H, J = 7.0 Hz), 7.88 (d, 1H, J = 7.9 Hz), 7.78 (t, 1H, J = 6.2 Hz), 7.63 (br m, 1H), 7.44 (d, 2H, J = 7.9 Hz), 2.42 (s, 3H). $^{13}C\{^1H\}$ NMR (DMSO-d_6, 101 MHz) δ 197.5 (CO), 194.0 (CO), 190.4 (CO), 161.6, 158.0, 157.2, 156.4, 152.8, 150.4, 149.2, 141.2, 139.9, 137.0, 131.7, 130.0, 127.7, 127.5, 125.5, 125.0, 124.9, 124.0, 120.2, 21.0. ATR-IR (ν_{CO}/cm^{-1}): 2021, 1934, 1898. UV–Vis {λ_{max}/nm (10^3 ε/L mol^{-1} cm^{-1})}: in acetonitrile: 268 (28.6), 301 (29.3), 379 (4.91); in DMF: 307 (23.9), 382 (4.30). HRMS (ESI-MS): calcd for $[M + H^+]$ 674.0055, found $[M + H^+]$ 674.0067. Anal calcd (in %) for $C_{25}H_{17}BrN_3O_3Re$: C, 44.58, H, 2.54; N, 6.24. Found: C, 44.77; H, 2.23; N, 6.24.

This journal is © The Royal Society of Chemistry 2023

Open Access Article. Published on 03 2566. Downloaded on 6/2/2569 0:03:00.
This article is licensed under a Creative Commons Attribution-NonCommercial 3.0 Unported Licence.

Re4. In a Schlenk flask, **L4** (47.8 mg, 0.123 mmol) and $Re(CO)_5Br$ (50.0 mg, 0.123 mmol) were dissolved in dry toluene refluxed for 4 h. After filtration and vacuum drying, an orange-coloured powder was obtained with a 98% yield (89.0 mg, 0.121 mmol). M.P.: >300 °C. ^{1}H NMR ($CDCl_3$, 500 MHz) δ (ppm): 9.14 (d, 1H, J = 5.48 Hz), 8.84 (d, 1H, J = 4.64 Hz), 8.36 (s, 1H, merged with another signal), 8.35 (d, 1H, merged with another signal), 8.09 (t, 1H, J = 7.78 Hz), 7.94 (t, 2H, J = 6.32 Hz), 7.88 (s, 1H), 7.71 (d, 2H, J = 8.52 Hz), 7.63 (d, 2H, J = 8.60 Hz), 7.58–7.50 (m, 2H). ^{1}H NMR (DMSO-d_6, 400 MHz) δ (ppm): 9.13 (s, 1H, merged with a doublet), 9.09 (d, J = 5.2 Hz, 1H, merged with a singlet), 8.80 (d, J = 3.2 Hz, 1H), 8.39 (t, J = 7.5 Hz, 1H), 8.22 (d, J = 5.3 Hz, 2H), 8.19 (s, 1H), 8.07 (t, J = 7.1 Hz, 1H), 7.90 (d, J = 7.6 Hz, 1H), 7.84 (d, J = 8.4 Hz, 2H), 7.79 (t, J = 6.4 Hz, 1H), 7.63 (t, J = 5.8 Hz, 1H). ^{13}C{^{1}H} NMR (DMSO-d_6, 101 MHz) δ (ppm): 197.5 (^{13}CO), 194.0 (^{13}CO), 190.5 (^{13}CO), 161.7, 158.0, 157.4, 156.4, 152.9, 150.7, 149.3, 140.0, 137.1, 134.8, 131.1, 129.5, 127.9, 127.6, 125.6, 125.1, 125.1, 124.5, 120.7. ATR-IR (ν_{CO}/cm^{-1}): 2019, 1909, 1880. UV–Vis {λ_{max}/nm (10^3 ε/L mol^{-1} cm^{-1})}: in acetonitrile: 269 (53.7), 297 (54.4), 378 (8.50); in DMF: 305 (32.6), 388 (5.84). HRMS (m/z): calcd for [M + H$^+$] 739.9003, found [M + H$^+$] 739.8991. Anal calcd (in %) for $C_{24}H_{14}Br_2N_3O_3Re$: C, 39.08; H, 1.91; N, 5.70. Found: C, 39.42; H, 1.56; N, 5.72.

Re5. In a Schlenk flask, **L5** (51.3 mg, 0.123 mmol) and $Re(CO)_5Br$ (50.0 mg, 0.123 mmol) were dissolved in dry toluene and refluxed for 4 h. The reaction mixture was allowed to cool to room temperature. After storing the solution at 4 °C for 24 h, a dark red coloured precipitate formed that was filtered, washed with cold diethyl ether and dried in air (53 mg). More precipitate (25 mg) was obtained by reducing the supernatant organic solvents to 1 mL in a rotary evaporator (100 mbar, 45 °C, 1 h) and adding cold diethyl ether. The combined precipitate was air dried, giving a dark, red-coloured powder with a total 74% yield (78.0 mg, 0.096 mmol, MW = 813; $C_{28}H_{19}N_3O_3BrFeRe{\cdot}xCH_3C_6H_5$, where x = 0.5). The compound was 96.4% pure as determined by RP-HPLC. M.P.: >300 °C. ^{1}H NMR ($CDCl_3$, 400 MHz) δ (ppm): 9.12 (br, 1H), 8.85 (d, 1H, J = 3.35 Hz), 8.28 (t, 1H, J = 8.0 Hz), 8.11 (br, 1H), 8.06 (t, 1H, J = 7.70 Hz), 7.91 (br d, 1H, J = 7.9 Hz), 7.66 (s, 1H), 7.51 (d, 2H, J = 6.69 Hz), 7.24 (merged with $CDCl_3$, 1H, toluene), 7.18 (d, J = 7.64 Hz, 1.4H, toluene), 4.90 (br s, 1H), 4.85 (br s, 1H), 4.62 (br s, 2H), 4.14 (s, 5H), 2.36 (s, 1.6H, toluene). ^{13}C{^{1}H} NMR (100 MHz, $CDCl_3$) δ (ppm): 158.2, 156.5, 154.2, 153.1, 149.6, 138.5, 137.0 (toluene, C), 129.0 (toluene, CH), 128.3 (toluene, CH), 126.3, 125.3 (toluene, CH), 124.8, 123.9, 118.8, 72.1, 72.0, 70.5, 68.2, 67.5, 21.5 (toluene, CH_3) (CO peaks are not visible). ^{1}H NMR (DMSO-d_6, 400 MHz) δ (ppm): 9.05 (s, 2H), 8.77 (bs, 2H), 8.38 (s, 1H), 8.04 (s, 1H), 7.84 (merged d, 3H), 7.62 (s, 1H), 7.21 (merged, 2.6H, toluene), 5.45 (s, 2H), 4.70 (s, 2H), 4.15 (s, 5H), 2.30 (s, 2H, toluene). ^{13}C{^{1}H} NMR (DMSO-d_6, 101 MHz) δ (ppm): 198.0 (CO), 194.6 (CO), 191.2 (CO), 161.1, 158.5, 157.2, 156.9, 154.9, 153.2, 149.7, 140.3, 137.8 (toluene, C), 137.4, 129.4 (toluene, CH), 128.7 (toluene, CH), 127.6, 125.9 (toluene, CH), 125.6, 125.5, 125.3, 123.2, 119.9, 78.2, 72.5, 70.8, 69.0, 68.6, 21.5 (toluene, CH_3). ATR-IR (ν_{CO}/cm^{-1}): 2013, 1904, 1886. UV–Vis {λ_{max}/nm (10^3 ε/L mol^{-1} cm^{-1})}: in acetonitrile 256 (23.4), 310 (21.8), 367 (5.02), 516 (2.35); in DMF: 311 (42.1), 370 (10.6), 516 (5.62). RP-HPLC: 1.989 min, 96.4% pure (acetonitrile and 1% ammonium formate in water) 95 : 5 (v/v). ESI-MS (m/z): 768 (expected 767, (M + H$^+$), $C_{28}H_{20}BrFeN_3O_3Re^+$) and 688 (expected 688, (M − Br$^+$), $C_{28}H_{19}FeN_3O_3Re^+$). HRMS (m/z): calcd for [M + Na$^+$] 789.9394, found [M + Na$^+$] 789.9397 and calcd for [M − Br]$^+$ 688.0352, found [M − Br]$^+$ 688.0422. Anal calcd (in %) for $C_{28}H_{19}BrFeN_3O_3Re$: C, 43.81; H, 2.50; N, 5.48. Found: C, 43.71; H, 2.51; N, 5.43.

Computational details

All the structures were optimised using B3LYP functional[93–95] using the ORCA package.[96] The def2-TZVP basis set is used for the optimisation.[97] The optimisations were carried out in an implicit solvent using the SMD solvent model,[98] with parameters corresponding to acetonitrile used to mimic the experimental conditions. The natures of the stationary points were characterised by frequency calculations at the same level of theory using the Gaussian 16 package.[99] Time-dependent density functional theory (TDDFT) calculations were carried out at the B3LYP/def2-TZVP level to calculate the absorption spectra of all the complexes using the ORCA package. The lowest 50 transitions were taken into account in the calculations of the absorption spectra.

Transient absorption spectroscopy

The ultrafast transient absorption (TA) was performed on a transient absorption spectrometer (Ultrafast Systems, USA). The pump pulses of 320 nm were generated from an OPerA Solo OPA (Coherent, USA) pumped by 35 fs, 5 mJ per pulse, and centred at 800 nm operating at 1 kHz generated from an Astrella amplified laser system (Coherent, USA). A part of the amplified output is used to generate broadband (340 to 680 nm) probe pulses by focusing it on the CaF_2 window. The transmission of the probe in the presence and absence of a pump was recorded on a CCD spectrograph using a synchronised mechanical chopper operating at 500 Hz. All samples were prepared in freshly distilled acetonitrile (HPLC, Spectrochem). The pump and probe polarisations are kept vertical with respect to each other. The OD of the samples were maintained at around 0.5 at the excitation wavelength in a 2 mm path length cuvette. The samples were stirred continuously using a magnetic stirrer throughout the experiment. The sample integrity was checked by recording its steady-state spectra before and after the experiment. The obtained transient absorption spectra were analysed using Surface Xplorer (V 4.0) and Origin 2019.

Electrochemistry

Electrochemical analysis was performed using a CH760E potentiostat or a BioLogic VSP potentiostat. Cyclic voltammetry measurements were performed in a one-compartment three-electrode setup using a glassy carbon working electrode (3 mm diameter), a platinum wire as the auxiliary electrode, and a

Open Access Article. Published on 03 2566. Downloaded on 6/2/2569 0:03:00.
This article is licensed under a Creative Commons Attribution-NonCommercial 3.0 Unported Licence.

non-aqueous $Ag|Ag^+$ pseudo-reference electrode, $Ag|AgNO_3$ (10 mM) in 0.1 M n-Bu_4NBF_4 in acetonitrile (or DMF). The voltammograms were referenced by the addition of ferrocene as an internal standard after the final experiment, and all potentials given in this work are reported against the $Fc^{+/0}$ couple. The potential of the $Fc^{+/0}$ couple was found to be ~0.07 V *vs.* the non-aqueous $Ag|Ag^+$ pseudo-reference. The supporting electrolyte was n-Bu_4NBF_4 (0.1 M), which was purified by recrystallisation from 1 : 2 ethanol/water followed by drying at 80 °C in a vacuum oven.

The diffusion coefficients (D) were determined by the Randles–Sevcik equation shown below:

$$i_p = 0.4463nFAC\left(\frac{nF\nu D}{RT}\right)^{1/2}$$

where i_p is the peak current under N_2, F is Faraday's constant, A is the surface area of the electrode (0.071 cm^2 for the glassy carbon electrode used here), n is the number of electrons associated with the redox event, C is the concentration of the catalyst in solution, ν is the scan rate, R is the ideal gas constant, and T is the temperature in Kelvin. Peak currents for the first reduction (n = 1) were plotted against the square root of the scan rates and the slope of the linear fit was used to determine D.

The observed rate constant (k_{obs}) was calculated using the following equation:

$$k_{obs} = \left(\frac{F\nu}{RT}\right)\left(\frac{0.4463}{n_{cat}}\right)^2\left(\frac{i_{cat}}{i_p}\right)^2$$

where ν = scan rate (V s^{-1}), RT/F = 0.0256 V (T = 298 K), n_{cat} = 2 (number of electrons required for the conversion of CO_2 to CO), i_{cat} = plateau current under CO_2 saturated conditions, and i_p = reduction peak current under N_2.

Controlled potential electrolysis

Controlled potential electrolysis measurements were performed in a custom two-compartment cell separated by a glass frit. A glassy carbon plate (2 mm thick Sigradur G-plates from HTW GmbH, Germany) was used as the working electrode, Pt mesh as the counterelectrode, and non-aquoeus Ag/Ag^+ as the reference. The effective geometric surface area of the electrode during electrolysis was 2 cm^2. Typically, the volumes of electrolytes in the working and counter compartments were 6 mL and 2 mL, respectively, with a headspace volume of 23 mL. The concentration of the catalyst during electrolysis was 0.25 mM.

The quantification of H_2 and CO was conducted using an SRI gas chromatograph (multiple gas analyser #1) equipped with a thermal conductivity detector (TCD) and a flame ionisation detector (FID) with a built-in methaniser attachment. A silica gel column (6 ft) column was used to block CO_2 and H_2O, and a molecular sieve 13X (6 ft) main column was used to separate the H_2, and CO. N_2 was used as the carrier gas. The GC was calibrated regularly using a known standard for H_2, CO and CH_4 (2000 ppm H_2/2000 ppm CO/2000 ppm CH_4 in balance gas N_2).

Spectroelectrochemistry

Spectroelectrochemical analysis was performed in a thin-layer quartz glass cuvette (path length 1 mm) using a Pt mesh working electrode, $Ag|Ag^+$ pseudo-reference electrode, and a Pt wire counterelectrode. An AvaLight-DHC (deuterium and halogen light source) was used as the light source, and the spectra were recorded using an AvaSpec-2048 spectrometer. The electrode was held at a set potential for 2 min before recording the UV-Vis spectrum.

Author contributions

RM conceived and supervised the project. SS synthesised and characterised all ligands and Re(I) complexes and observed the initial CO_2 reduction. TD and SR performed electrocatalysis and spectroelectrochemical experiments. DB and DM performed the computational studies. SKP and ESSI carried out ultrafast transient absorption spectroscopy. The manuscript was written through contributions from all authors. All authors have approved the final version of the manuscript.

Conflicts of interest

There are no conflicts of interest to declare.

Acknowledgements

SS, RM, SKP and ESSI thank Indian Institute of Technology Goa (IIT Goa) for the infrastructure and teaching assistant fellowship. RM thanks SERB for the initial funding through a start-up research grant (SERB SRG/2019/000604). TD and SR acknowledge support from the EPSRC Doctoral Training Program (EP/T518177/1) and the Royal Society (RGS\R2 \202350). DM acknowledges the National Supercomputing Mission (DST/NSM/R&D_HPC_Applications/2021/08) for providing computing resources of 'PARAM Shakti' at the Indian Institute of Technology Kharagpur (IIT Kgp) and 'PARAM Brahma' at IISER Pune, which are implemented by C-DAC and supported by the Ministry of Electronics and Information Technology (MeitY) and Department of Science and Technology (DST), Government of India. SERB SRG/2019/000604; EPSRC EP/T518177/1.

References

1 T. R. Anderson, E. Hawkins and P. D. Jones, *Endeavour*, 2016, **40**, 178–187.
2 I. P. on C. C. W. G. 1 Science, I. P. on C. Change and I. P. on C. C. W. G. I, *Climate Change 2007 - The Physical Science Basis: Working Group I Contribution to the Fourth Assessment Report of the IPCC*, Cambridge University Press, 2007.

This journal is © The Royal Society of Chemistry 2023

Open Access Article. Published on 03 2566. Downloaded on 6/2/2569 0:03:00.
This article is licensed under a Creative Commons Attribution-NonCommercial 3.0 Unported Licence.

3 Climate Change 2022, https://www.ipcc.ch/report/ar6/wg3/, (accessed 3 October 2022).
4 B. Obama, *Science*, 2017, **355**, 126–129.
5 J. L. Sarmiento, T. M. C. Hughes, R. J. Stouffer and S. Manabe, *Nature*, 1998, **393**, 245–249.
6 G. Centi and S. Perathoner, *Green Chem.*, 2022, **24**, 7305–7331.
7 J. K. Nganga, L. M. Wolf, K. Mullick, E. Reinheimer, C. Saucedo, M. E. Wilson, K. A. Grice, M. Z. Ertem and A. M. Angeles-Boza, *Inorg. Chem.*, 2021, **60**, 3572–3584.
8 Y. Yang and J.-W. Lee, *Chem. Sci.*, 2019, **10**, 3905–3926.
9 N. W. Kinzel, C. Werlé and W. Leitner, *Angew. Chem., Int. Ed.*, 2021, **60**, 11628–11686.
10 H.-Q. Liang, T. Beweries, R. Francke and M. Beller, *Angew. Chem., Int. Ed.*, 2022, **61**, e202200723.
11 R. Francke, B. Schille and M. Roemelt, *Chem. Rev.*, 2018, **118**, 4631–4701.
12 D. Grammatico, A. J. Bagnall, L. Riccardi, M. Fontecave, B.-L. Su and L. Billon, *Angew. Chem., Int. Ed.*, 2022, **61**, e202206399.
13 K. Lei and B. Y. Xia, *Chem. – Eur. J.*, 2022, **28**, e202200141.
14 J. P. Collin and J. P. Sauvage, *Coord. Chem. Rev.*, 1989, **93**, 245–268.
15 F.-Y. Gao, R.-C. Bao, M.-R. Gao and S.-H. Yu, *J. Mater. Chem. A*, 2020, **8**, 15458–15478.
16 W. Nie and C. C. L. McCrory, *Dalton Trans.*, 2022, **51**, 6993–7010.
17 S. Roy, B. Sharma, J. Pécaut, P. Simon, M. Fontecave, P. D. Tran, E. Derat and V. Artero, *J. Am. Chem. Soc.*, 2017, **139**, 3685–3696.
18 C. Costentin, S. Drouet, M. Robert and J.-M. Savéant, *Science*, 2012, **338**, 90–94.
19 M. Wang, K. Torbensen, D. Salvatore, S. Ren, D. Joulié, F. Dumoulin, D. Mendoza, B. Lassalle-Kaiser, U. Işci, C. P. Berlinguette and M. Robert, *Nat. Commun.*, 2019, **10**, 3602.
20 A. Chapovetsky, T. H. Do, R. Haiges, M. K. Takase and S. C. Marinescu, *J. Am. Chem. Soc.*, 2016, **138**, 5765–5768.
21 B. Siritanaratkul, C. Eagle and A. J. Cowan, *Acc. Chem. Res.*, 2022, **55**, 955–965.
22 M. R. Madsen, M. H. Rønne, M. Heuschen, D. Golo, M. S. G. Ahlquist, T. Skrydstrup, S. U. Pedersen and K. Daasbjerg, *J. Am. Chem. Soc.*, 2021, **143**, 20491–20500.
23 M. Boraghi, T. A. White, S. Pordel and H. Payne, *ACS Appl. Energy Mater.*, 2021, **4**, 13725–13734.
24 M. Guyot, M.-N. Lalloz, J. S. Aguirre-Araque, G. Rogez, C. Costentin and S. Chardon-Noblat, *Inorg. Chem.*, 2022, **61**, 16072–16080.
25 C. J. Stanton, C. W. Machan, J. E. Vandezande, T. Jin, G. F. Majetich, H. F. Schaefer, C. P. Kubiak, G. Li and J. Agarwal, *Inorg. Chem.*, 2016, **55**, 3136–3144.
26 J. Mukherjee and I. Siewert, *Eur. J. Inorg. Chem.*, 2020, **2020**, 4319–4333.
27 E. Quartapelle Procopio, A. Boni, L. Veronese, M. Marcaccio, P. Mercandelli, G. Valenti, M. Panigati and F. Paolucci, *ChemElectroChem*, 2021, **8**, 2065–2069.
28 M. Bourrez, F. Molton, S. Chardon-Noblat and A. Deronzier, *Angew. Chem., Int. Ed.*, 2011, **50**, 9903–9906.
29 H. Koizumi, H. Chiba, A. Sugihara, M. Iwamura, K. Nozaki and O. Ishitani, *Chem. Sci.*, 2019, **10**, 3080–3088.
30 J. M. Smieja and C. P. Kubiak, *Inorg. Chem.*, 2010, **49**, 9283–9289.
31 F. P. A. Johnson, M. W. George, F. Hartl and J. J. Turner, *Organometallics*, 1996, **15**, 3374–3387.
32 M. Wrighton and D. L. Morse, *J. Am. Chem. Soc.*, 1974, **96**, 998–1003.
33 L. Rotundo, C. Garino, E. Priola, D. Sassone, H. Rao, B. Ma, M. Robert, J. Fiedler, R. Gobetto and C. Nervi, *Organometallics*, 2019, **38**, 1351–1360.
34 L. Rotundo, D. E. Polyansky, R. Gobetto, D. C. Grills, E. Fujita, C. Nervi and G. F. Manbeck, *Inorg. Chem.*, 2020, **59**, 12187–12199.
35 C. Riplinger and E. A. Carter, *ACS Catal.*, 2015, **5**, 900–908.
36 M. L. Clark, P. L. Cheung, M. Lessio, E. A. Carter and C. P. Kubiak, *ACS Catal.*, 2018, **8**, 2021–2029.
37 S. E. Tignor, H.-Y. Kuo, T. S. Lee, G. D. Scholes and A. B. Bocarsly, *Organometallics*, 2019, **38**, 1292–1299.
38 C. Jiang, A. W. Nichols and C. W. Machan, *Dalton Trans.*, 2019, **48**, 9454–9468.
39 S. Amanullah, P. Saha, A. Nayek, M. E. Ahmed and A. Dey, *Chem. Soc. Rev.*, 2021, **50**, 3755–3823.
40 W. L. J. Loke, W. Guo, M. Sohail, A. A. Bengali and W. Y. Fan, *Inorg. Chem.*, 2022, **61**, 20699–20708.
41 K. Talukdar, S. Sinha Roy, E. Amatya, E. A. Sleeper, P. Le Magueres and J. W. Jurss, *Inorg. Chem.*, 2020, **59**, 6087–6099.
42 S. Sinha Roy, K. Talukdar and J. W. Jurss, *ChemSusChem*, 2021, **14**, 662–670.
43 A. N. Hellman, J. A. Intrator, J. C. Choate, D. A. Velazquez and S. C. Marinescu, *Polyhedron*, 2022, **223**, 115933.
44 A. N. Hellman, R. Haiges and S. C. Marinescu, *ChemElectroChem*, 2021, **8**, 1864–1872.
45 S. Sung, D. Kumar, M. Gil-Sepulcre and M. Nippe, *J. Am. Chem. Soc.*, 2017, **139**, 13993–13996.
46 E. Haviv, D. Azaiza-Dabbah, R. Carmieli, L. Avram, J. M. L. Martin and R. Neumann, *J. Am. Chem. Soc.*, 2018, **140**, 12451–12456.
47 J. O. Taylor, G. Neri, L. Banerji, A. J. Cowan and F. Hartl, *Inorg. Chem.*, 2020, **59**, 5564–5578.
48 C. C. Addison, R. Davis and N. Logan, *J. Chem. Soc., Dalton Trans.*, 1974, 2070–2071.
49 N. Elgrishi, M. B. Chambers, X. Wang and M. Fontecave, *Chem. Soc. Rev.*, 2017, **46**, 761–796.
50 T. Yoshida, K. Tsutsumida, S. Teratani, K. Yasufuku and M. Kaneko, *J. Chem. Soc., Chem. Commun.*, 1993, 631–633.
51 S. Sinha, A. Sonea, C. A. Gibbs and J. J. Warren, *Dalton Trans.*, 2020, **49**, 7078–7083.
52 E. W. Abel, N. J. Long, K. G. Orrell, A. G. Osborne, H. M. Pain and V. Šik, *J. Chem. Soc., Chem. Commun.*, 1992, 303–304.
53 K. Choroba, S. Kotowicz, A. Maroń, A. Świtlicka, A. Szłapa-Kula, M. Siwy, J. Grzelak, K. Sulowska, S. Maćkowski,

Open Access Article. Published on 03 2566. Downloaded on 6/2/2569 0:03:00.
This article is licensed under a Creative Commons Attribution-NonCommercial 3.0 Unported Licence.

E. Schab-Balcerzak and B. Machura, *Dyes Pigm.*, 2021, **192**, 109472.
54 A. P. Sadimenko, in *Advances in Heterocyclic Chemistry*, ed. A. R. Katritzky, Academic Press, 2007, vol. 94, pp. 107–172.
55 R. Fernández-Terán and L. Sévery, *Inorg. Chem.*, 2021, **60**, 1334–1343.
56 R. J. Fernández-Terán and L. Sévery, *Inorg. Chem.*, 2021, **60**, 1325–1333.
57 K. Choroba, A. Maroń, A. Świtlicka, A. Szłapa-Kula, M. Siwy, J. Grzelak, S. Maćkowski, T. Pedzinski, E. Schab-Balcerzak and B. Machura, *Dalton Trans.*, 2021, **50**, 3943–3958.
58 M. Małecka, A. Szlapa-Kula, A. M. Maroń, P. Ledwon, M. Siwy, E. Schab-Balcerzak, K. Sulowska, S. Maćkowski, K. Erfurt and B. Machura, *Inorg. Chem.*, 2022, **61**, 15070–15084.
59 J. Wang and G. S. Hanan, *Synlett*, 2005, 1251–1254.
60 A. Gelling, K. G. Orrell, A. G. Osborne and V. Šik, *J. Chem. Soc., Dalton Trans.*, 1998, 937–946.
61 S. A. Moya, R. Pastene, H. Le Bozec, P. J. Baricelli, A. J. Pardey and J. Gimeno, *Inorg. Chim. Acta*, 2001, **312**, 7–14.
62 G. R. Fulmer, A. J. M. Miller, N. H. Sherden, H. E. Gottlieb, A. Nudelman, B. M. Stoltz, J. E. Bercaw and K. I. Goldberg, *Organometallics*, 2010, **29**, 2176–2179.
63 T. Auvray, B. Del Secco, A. Dubreuil, N. Zaccheroni and G. S. Hanan, *Inorg. Chem.*, 2021, **60**, 70–79.
64 M. Feng, F. Yang and J. Wang, *Chin. J. Chem. Phys.*, 2016, **29**, 81–86.
65 A. El Nahhas, A. Cannizzo, F. Van Mourik, A. M. Blanco-Rodríguez, S. Záliš, A. Vlček and M. Chergui, *J. Phys. Chem. A*, 2010, **114**, 6361–6369.
66 A. M. Maroń, A. Szlapa-Kula, M. Matussek, R. Kruszynski, M. Siwy, H. Janeczek, J. Grzelak, S. Maćkowski, E. Schab-Balcerzak and B. Machura, *Dalton Trans.*, 2020, **49**, 4441–4453.
67 A. N. Tarnovsky, W. Gawelda, M. Johnson, C. Bressler and M. Chergui, *J. Phys. Chem. B*, 2006, **110**, 26497–26505.
68 A. El Nahhas, A. Cannizzo, F. van Mourik, A. M. Blanco-Rodríguez, S. Záliš, A. Vlček Jr. and M. Chergui, *J. Phys. Chem. A*, 2010, **114**, 6361–6369.
69 J. Palion-Gazda, A. Szłapa-Kula, M. Penkala, K. Erfurt and B. Machura, *Molecules*, 2022, **27**, 7147.
70 R. Fernández-Terán and L. Sévery, *Inorg. Chem.*, 2021, **60**, 1334–1343.
71 A. Szlapa-Kula, M. Małecka, A. M. Maroń, H. Janeczek, M. Siwy, E. Schab-Balcerzak, M. Szalkowski, S. Maćkowski, T. Pedzinski, K. Erfurt and B. Machura, *Inorg. Chem.*, 2021, **60**, 18726–18738.
72 O. F. Mohammed and A. A. O. Sarhan, *Chem. Phys.*, 2010, **372**, 17–21.
73 A. J. King, Y. V. Zatsikha, T. Blessener, F. Dalbec, P. C. Goff, M. Kayser, D. A. Blank, Y. P. Kovtun and V. N. Nemykin, *J. Organomet. Chem.*, 2019, **887**, 86–97.
74 J. Palion-Gazda, A. Szłapa-Kula, M. Penkala, K. Erfurt and B. Machura, *Molecules*, 2022, **27**, 7147.
75 K. Choroba, A. Maroń, A. Świtlicka, A. Szłapa-Kula, M. Siwy, J. Grzelak, S. Maćkowski, T. Pedzinski, E. Schab-Balcerzak and B. Machura, *Dalton Trans.*, 2021, **50**, 3943–3958.
76 T. R. O'Toole, L. D. Margerum, T. D. Westmoreland, W. J. Vining, R. W. Murray and T. J. Meyer, *J. Chem. Soc., Chem. Commun.*, 1985, 1416–1417.
77 B. P. Sullivan, C. M. Bolinger, D. Conrad, W. J. Vining and T. J. Meyer, *J. Chem. Soc., Chem. Commun.*, 1985, 1414–1416.
78 P. Christensen, A. Hamnett, A. V. G. Muir and J. A. Timney, *J. Chem. Soc., Dalton Trans.*, 1992, 1455–1463.
79 A. N. Hellman, R. Haiges and S. C. Marinescu, *Dalton Trans.*, 2019, **48**, 14251–14255.
80 E. S. Rountree, B. D. McCarthy, T. T. Eisenhart and J. L. Dempsey, *Inorg. Chem.*, 2014, **53**, 9983–10002.
81 C. Costentin and J.-M. Savéant, *ChemElectroChem*, 2014, **1**, 1226–1236.
82 C. Costentin, S. Drouet, M. Robert and J.-M. Savéant, *J. Am. Chem. Soc.*, 2012, **134**, 11235–11242.
83 C. J. Bondue, M. Graf, A. Goyal and M. T. M. Koper, *J. Am. Chem. Soc.*, 2021, **143**, 279–285.
84 J. T. Muckerman, J. H. Skone, M. Ning and Y. Wasada-Tsutsui, *Biochim. Biophys. Acta, Bioenerg.*, 2013, **1827**, 882–891.
85 A. G. Al-Sehemi, A. Irfan, A. M. Asiri and Y. A. Ammar, *Spectrochim. Acta, Part A*, 2012, **91**, 239–243.
86 S. Vaduvescu and P. G. Potvin, *Eur. J. Inorg. Chem.*, 2004, **2004**, 1763–1769.
87 M. N. Patel, P. A. Parmar and D. S. Gandhi, *J. Enzyme Inhib. Med. Chem.*, 2011, **26**, 734–741.
88 A. Juneja, T. S. Macedo, D. R. M. Moreira, M. B. P. Soares, A. C. L. Leite, J. K. de A. L. Neves, V. R. A. Pereira, F. Avecilla and A. Azam, *Eur. J. Med. Chem.*, 2014, **75**, 203–210.
89 P. Bulsink, A. Al-Ghamdi, P. Joshi, I. Korobkov, T. Woo and D. Richeson, *Dalton Trans.*, 2016, **45**, 8885–8896.
90 T. Klemens, A. Świtlicka, A. Szlapa-Kula, S. Krompiec, P. Lodowski, A. Chrobok, M. Godlewska, S. Kotowicz, M. Siwy, K. Bednarczyk, M. Libera, S. Maćkowski, T. Pędziński, E. Schab-Balcerzak and B. Machura, *Appl. Organomet. Chem.*, 2018, **32**, e4611.
91 T. Klemens, A. Świtlicka-Olszewska, B. Machura, M. Grucela, H. Janeczek, E. Schab-Balcerzak, A. Szlapa, S. Kula, S. Krompiec, K. Smolarek, D. Kowalska, S. Mackowski, K. Erfurt and P. Lodowski, *RSC Adv.*, 2016, **6**, 56335–56352.
92 E. W. Abel, V. S. Dimitrov, N. J. Long, K. G. Orrell, A. G. Osborne, H. M. Pain, V. Šik, M. B. Hursthouse and M. A. Mazid, *J. Chem. Soc., Dalton Trans.*, 1993, 597–603.
93 A. D. Becke, *Phys. Rev. A*, 1988, **38**, 3098–3100.
94 A. D. Becke, *J. Chem. Phys.*, 1992, **96**, 2155–2160.
95 A. D. Becke, *J. Chem. Phys.*, 1993, **98**, 5648–5652.
96 F. Neese, *Wiley Interdiscip. Rev.: Comput. Mol. Sci.*, 2012, **2**, 73–78.
97 F. Weigend and R. Ahlrichs, *Phys. Chem. Chem. Phys.*, 2005, **7**, 3297–3305.
98 A. V. Marenich, C. J. Cramer and D. G. Truhlar, *J. Phys. Chem. B*, 2009, **113**, 6378–6396.

This journal is © The Royal Society of Chemistry 2023

Open Access Article. Published on 03 2566. Downloaded on 6/2/2569 0:03:00.
This article is licensed under a Creative Commons Attribution-NonCommercial 3.0 Unported Licence.

99 M. J. Frisch, G. W. Trucks, H. B. Schlegel, G. E. Scuseria, M. A. Robb, J. R. Cheeseman, G. Scalmani, V. Barone, G. A. Petersson, H. Nakatsuji, X. Li, M. Caricato, A. V. Marenich, J. Bloino, B. G. Janesko, R. Gomperts, B. Mennucci, H. P. Hratchian, J. V. Ortiz, A. F. Izmaylov, J. L. Sonnenberg, D. Williams-Young, F. Ding, F. Lipparini, F. Egidi, J. Goings, B. Peng, A. Petrone, T. Henderson, D. Ranasinghe, V. G. Zakrzewski, J. Gao, N. Rega, G. Zheng, W. Liang, M. Hada, M. Ehara, K. Toyota, R. Fukuda, J. Hasegawa, M. Ishida, T. Nakajima, Y. Honda, O. Kitao, H. Nakai, T. Vreven, K. Throssell, J. A. Montgomery Jr., J. E. Peralta, F. Ogliaro, M. J. Bearpark, J. J. Heyd, E. N. Brothers, K. N. Kudin, V. N. Staroverov, T. A. Keith, R. Kobayashi, J. Normand, K. Raghavachari, A. P. Rendell, J. C. Burant, S. S. Iyengar, J. Tomasi, M. Cossi, J. M. Millam, M. Klene, C. Adamo, R. Cammi, J. W. Ochterski, R. L. Martin, K. Morokuma, O. Farkas, J. B. Foresman and D. J. Fox, *Gaussian 16, Revision C.01*, Gaussian, Inc., Wallingford CT, 2016.